

# 國立交通大學

## 物理研究所

### 博士論文

量子力學在動量空間的表象及其在鋰原子的強場游離之應用

Momentum Representation in Quantum Mechanics with Application to  
Strong-field Ionization of Lithium Atom



研究生：鄭世達

指導教授：江進福 教授

程思誠 教授

中華民國一零二年七月

# 量子力學在動量空間的表象及其在鋰原子的強場游離之應用

## Momentum Representation in Quantum Mechanics with Application to Strong-field Ionization of Lithium Atom

研究生：鄭世達

Student : Shih-Da Jheng

指導教授：江進福

Advisor : Tsing-Fu Jiang

程思誠

Szu-Cheng Cheng



in partial Fulfillment of the Requirements

for the Degree of

Doctor of Philosophy

in

Physics

July 2013

Hsinchu, Taiwan, Republic of China

中華民國一零二年七月

# 量子力學在動量空間的表象及其在鋰原子的強場游離之應用

學生：鄭世達

指導教授：江進福  
程思誠

國立交通大學物理研究所博士班

## 摘 要

我們建立了一套準確且有效率的方法，去解原子和雷射交互作用在動量空間的表象的薛丁格方程式。我們的方法是建立在分離運算子方法(split-operator method)和有限積分範圍的蘭迪方法(Landé subtraction method with finite integration limits)之上。我們測試了包含線性偏極脈衝、圓形偏極脈衝和長波長脈衝的情況，我們的計算結果和其他計算方法得到的結果是一致的。我們也用有限積分範圍的蘭迪方法去推廣李文斯坦模型(Lewenstein model)。接下來，我們應用已建立的動量空間薛丁格方程式解法，去做鋰原子的強場游離的研究。在較低雷射強度的區域，經由分析相關的束縛態被佔據的歷史和將光電子頻譜(photoelectron spectra)分成奇數和偶數角動量部分，我們可以追溯出多光子游離(multiphoton ionization)在光電子頻譜形成的峰點的來源。在較強雷射強度的區域，我們指出了電子會穩定地停留在雷德堡態(Rydberg states)並解釋了為什麼游離電子明顯集中到垂直於雷射偏極的方向。

Momentum Representation in Quantum Mechanics  
with Application to Strong-field Ionization of Lithium Atom

student : Shih-Da Jheng

Advisors : Dr. Tsin-Fu Jiang  
Dr. Szu-Cheng Cheng

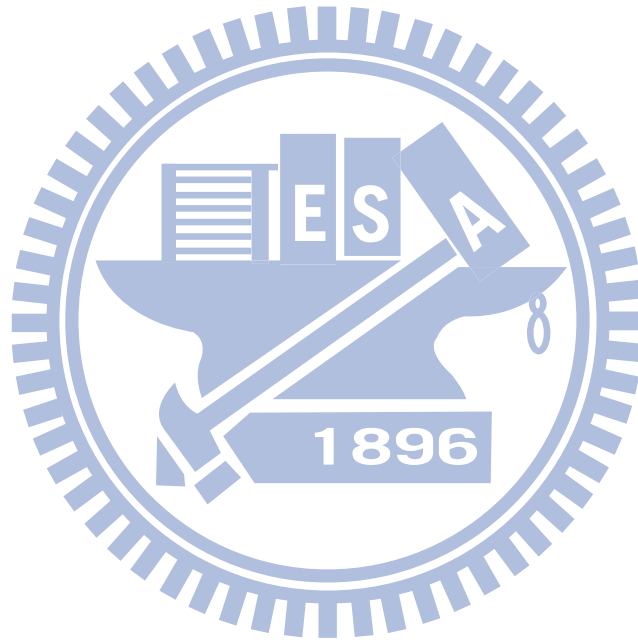
Institute of Physics  
National Chiao Tung University

ABSTRACT

We developed an accurate as well as efficient scheme to solve time-dependent Schrödinger equation in momentum space of an atom interacting with a laser pulse. Our scheme is based on split-operator method in energy representation and Landé subtraction method with finite integration limits. Cases of linearly polarized pulse, circularly polarized pulse, and long wavelength pulses are tested. Our results agree well with those from coordinate space calculations. We also apply the Landé subtraction method with finite integration limits to generalize Lewenstein model. Next, we use the developed P-space TDSE to study the strong-field ionization of a lithium atom with a linearly polarized pulse. By analyzing the population history of relevant bound states and separation the photoelectron spectra into odd and even angular momentum parts, we can trace the origin of multiphoton ionization peaks in the lower intensity regime. We point out the Rydberg stabilization and explain why the fan structure becomes evident in the direction perpendicular to the polarization axis in the higher intensity regime.

## 誌 謝

兩年前，我從沒想過我可以在今年完成我的博士論文，甚至，我一度覺得我可能無法完成我的博士學位，而現在竟然已經通過口試，在寫論文最後的誌謝部份了，到現在還是有點不可置信的感覺。首先，我要感謝我的指導老師江進福老師和程思誠老師，兩位老師對研究都非常熱忱，在他們的指導下，我從完全不懂到可以掌握一個領域的重點、學會研究過程中所需的技術並建立自己的工具、學著嚴謹地分析數據、還有從原本的不知所云到最後漸漸可以將結果較清楚地呈現出來並發表。這些教導與訓練，不僅僅只是科學研究上的訓練，廣義上來說，這是一個如何讓人可以將想法、創意具體實現的訓練過程，對於日後不論做什麼都有莫大的幫助。接著，感謝同研究室的博士後研究員李漢傑博士，李博士對人熱心，對研究非常熱忱，受到他在研究上非常多的幫助。再來，感謝在研究所一起打拼的同學、學弟，和大家一起吃飯聊天時，是苦悶的研究日子裡最輕鬆的時刻。最後要感謝我的爸爸、媽媽、姊姊，謝謝你們的支持，讓我可以一直做我想做的事情。



# Contents

<b>1</b>	<b>Introduction</b>	<b>1</b>
<b>2</b>	<b>Methods</b>	<b>5</b>
2.1	Time-dependent Schrödinger equation in momentum space (P-space TDSE) . . . . .	6
2.2	Landé subtraction method with finite integration limits . . . . .	10
2.3	Results of P-space TDSE . . . . .	16
2.3.1	Linear polarization case . . . . .	16
2.3.2	Elliptical polarization case . . . . .	19
2.4	Strong-field Approximation . . . . .	21
2.4.1	Keldysh-Faisal-Reiss (KFR) theory . . . . .	21
2.4.2	Lewenstein model . . . . .	22
2.4.3	Results . . . . .	23
<b>3</b>	<b>Strong-field Ionization of a Lithium Atom</b>	<b>27</b>
3.1	Compare with experimental results . . . . .	28
3.2	Features of strong-field ionization of a lithium atom . . . . .	34
3.3	Multiphoton ionization (MPI) . . . . .	41
3.3.1	Examination of the spectra for 30fs pulse . . . . .	43
3.3.2	Examination of the spectra for 10fs pulse . . . . .	44
3.4	Rydberg stabilization . . . . .	48
3.5	Fanlike structure in the direction perpendicular to the polarization axis . . . . .	52
<b>4</b>	<b>Conclusion</b>	<b>54</b>
	<b>Bibliography</b>	<b>56</b>
	<b>Appendix</b>	<b>61</b>
.1	Dipole approximation, velocity gauge, length gauge, and Volkov state . . . . .	61

# List of Figures

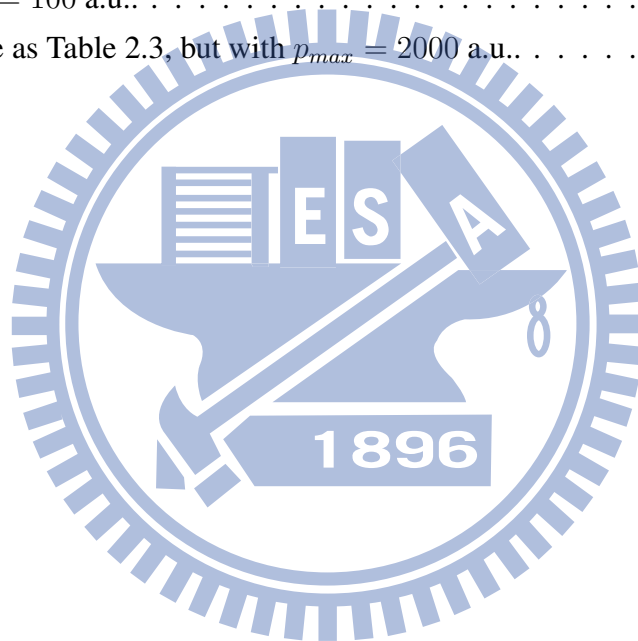
2.1	Comparison of the numerical wave functions with the exact ones. . . . .	15
2.2	Electric field $\mathbf{E}(t)$ and vector potential $\mathbf{A}(t)$ of a five-cycles pulse. . . . .	16
2.3	Comparison of the photoelectron spectra for $p_{max} = 100$ and $p_{max} = 10$ of a hydrogen atom with a linear polarized laser pulse. . . . .	17
2.4	Comparison of the two-dimensional momentum distribution of the same system as Fig. 2.3. . . . .	18
2.5	Comparison of the two-dimensional momentum distribution of a hydrogen atom with a linear polarized long wavelength laser pulse. . . . .	18
2.6	Comparison of the two-dimensional momentum distribution in the x-y plane of a hydrogen atom with a circular polarized laser pulse. . . . .	20
2.7	Photoelectron spectra of the TDSE as well as two versions of SFA results of a hydrogen atom with a linear polarized laser pulse. . . . .	24
2.8	Two-dimensional momentum distribution of TDSE and SFA1 of the same system as Fig. 2.7. . . . .	26
2.9	Energy-angular momentum distribution of TDSE and SFA1 of the same system as Fig. 2.7. . . . .	26
3.1	Iso-intensity surface plot of a laser-focal volume. . . . .	28
3.2	Two-dimensional momentum distribution of a lithium atom with a linear polarized laser pulse for lower intensities. . . . .	30
3.3	Two-dimensional momentum distribution of a lithium atom with a linear polarized laser pulse for higher intensities. . . . .	31
3.4	Photoelectron spectra of a lithium atom with a linear polarized laser pulse for lower intensities. . . . .	32
3.5	Photoelectron spectra of a lithium atom with a linear polarized laser pulse for higher intensities. . . . .	33
3.6	Energy levels of a lithium atom and the possible transition pathways. . . . .	34
3.7	Two-dimensional momentum distribution of a lithium atom with a linear polarized laser pulse with FWHM 30fs at a single peak intensity. . . . .	35

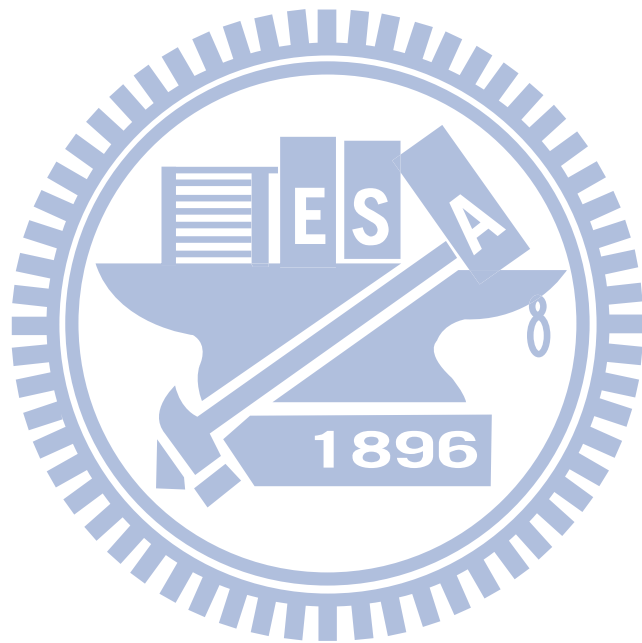
3.8	Photoelectron spectra of a lithium atom with a linear polarized laser pulse with FWHM 30fs at a single peak intensity. . . . .	36
3.9	Two-dimensional momentum distribution of a lithium atom with a linear polarized laser pulse with FWHM 10fs at single peak intensity. . . . .	37
3.10	Photoelectron spectra of a lithium atom with a linear polarized laser pulse with FWHM 10fs at a single peak intensity. . . . .	38
3.11	Ionization probability vs Keldysh parameter $\gamma$ . . . . .	40
3.12	Schematic plot of the NRMPI and DRMPI processes. . . . .	41
3.13	Separation of the photoelectron spectrum into the even and odd angular momentum parts. . . . .	43
3.14	Population history and photoelectron spectra of a lithium atom with a linear polarized laser pulse with FWHM 30fs and $40 \times 10^{11} W/cm^2$ . . . .	44
3.15	Population history and photoelectron spectra of a lithium atom with a linear polarized laser pulse with FWHM 10fs and $40 \times 10^{11} W/cm^2$ . . . .	45
3.16	transition from direct 4-photon ionization to direct 5-photon ionization. . .	46
3.17	Peak-position of the highest peak vs laser intensity. . . . .	47
3.18	Schematic plot of the process of transition from direct 4-photon ionization to direct 5-photon ionization. . . . .	49
3.19	Ionization probability, probability in low-lying states and probability in Rydberg states vs Keldysh parameter $\gamma$ . . . . .	50
3.20	Ratio of the sum of the occupation probability of the Rydberg states ( $n \geq 5$ ) to that of total bound states. . . . .	51
3.21	Two-dimensional momentum distribution of a lithium atom with a linear polarized laser pulse for three different intensities in the higher intensity regime. . . . .	53



# List of Tables

2.1	Numerical values of $I_l$ for $l=0-19$ . [56]. . . . .	12
2.2	Comparison of eigenvalues and wave functions of a hydrogen atom between "Present" Landé subtraction method method and "Ordinary" one for $p_{max} = 100$ a.u.. . . . .	13
2.3	The same as Table 2.3, but with $p_{max} = 2000$ a.u.. . . . .	13





# Chapter 1

## Introduction

Atomic ionization under strong laser field has been an attractive topic for decades. With the advance of the intense and short pulse laser technology, the study of the phenomena and corresponding applications of strong-field ionization continue to attract attention [1, 2]. Phenomena of an atom exposed to intense laser field include: multiphoton ionization (MPI), above-threshold ionization (ATI), tunneling ionization (TI), over-barrier ionization (OBI), and high-order harmonic generation (HHG).

MPI and ATI are associated processes. MPI is a process that a bound electron is ionized by absorbing enough photons successively to exceed the ionization potential. The ionized electron can continue to absorb more photons successively, then form evenly spaced multiplexes in the photoelectron spectra. The space between the two adjacent peaks is a photon energy. This is known as ATI [3, 4, 5, 6]. In a laser field, atomic potential can be suppressed by the laser field and form a potential barrier. Then, an electron ionized by tunneling through the barrier is known as TI. OBI occurs if the laser intensity is so high that the peak of the potential barrier is lower than the ground state energy.

In the aspect of light, if an intense laser with frequency  $\omega$  acts on atom samples, the spectra of the output light will contain odd multiple of  $\omega$ . This is known as HHG. This phenomenon can be understood by the three-step model [7]: (i) an electron is ionized through tunneling, (ii) the ionized electron is accelerated by the laser field, (iii) the electron is driven back by the laser field and recombines with the ion core. Then, emits high-order harmonic light and the cutoff is about  $I_p + 3Up$ , where  $I_p$  is the ionization potential of an atom and  $Up = I_0/4\omega^2$  is ponderomotive energy (or average kinetic energy) of a free electron in the laser field with intensity  $I_0$  and carrier frequency  $\omega$ .

The regime of MPI and TI can be classified conveniently by Keldysh parameter [8, 9], which is the ratio of tunneling time to the period of the laser wave. It is given by

$$\gamma = \sqrt{\frac{I_p}{2Up}} \quad (1.1)$$

$\gamma > 1$ , for lower laser intensity or larger frequency, is MPI regime. In this region, photoelectron spectra are dominant by nonresonant multiphoton ionization (NRMPI) and dynamical resonant multiphoton ionization (DRMPI) [10]. Many experimental electron spectra, especially rare gas atoms, have been carefully studied in this regime [11, 12, 13, 14].  $\gamma < 1$ , for higher intensity or smaller frequency, TI becomes dominant. This region has been investigated experimentally and theoretically but the interpretation of the data appears to be somewhat confusing so far [15, 16, 17, 18, 19, 20, 21]. Recent study in the mid-infrared regime reinforce such confusion [22, 23, 24, 25, 26, 27, 28]. And, to distinguish the TI signature in the photoelectron spectra is still an interested topic [29, 30, 31].

By an intense laser field we mean the energy scale of laser-atom interaction is comparable to the atomic binding energy. Therefore, perturbation theory is no longer valid. Nonperturbative treatment is needed. Two successful quantum mechanical theoretical tools that usually used to study the strong-field ionization are: numerical calculation of time-dependent Schrödinger equation (TDSE) and strong-field approximation (SFA) [7, 8, 32, 33]. Actually, SFA is still a perturbation theory but somewhat different from typical perturbation treatment. For initially bounded electron, laser field is treated as a perturbation. Once the electron is ionized, atomic potential become smaller for the distant electron and thus is taken as a perturbation. SFA is a two-fold perturbation theory. However, SFA can only give a qualitative description, but is still useful due to its clear physical picture and easily handling. Numerical calculation of TDSE is more convincing, but it become computationally more challenging for higher laser intensity or longer pulse duration.

There are many methods for numerical calculation of TDSE, such as split-operator method [34], matrix iteration method [35, 36], Arnoldi-Lanczos method [37], Kramers-Henneberger like transform method [38, 39], using integration form [40, 41], and the time-dependent surface flux method [42] etc. In these methods, calculations are performed in the coordinate space (R-space). In the numerical calculation, a finite box will be set in the space. Due to the more spreading character of the ionized wave function in the R-space, it is easy to reach the boundary of the box and will then be reflected. To avoid reflection, a filter function is usually used at the boundary. Wave function will be filtered out when reaching the box boundary. In this way, some information in the wave function will be also filtered out. Especially at higher laser intensity, a more larger box will be required to retain more information in the wave function, so do the grid points. Hence, make the R-space TDSE difficult to perform accurately and efficiently.

Uncertainty principle tells us the more spreading ionized wave function in the R-space, the more it is localized in the P-space. If performing the calculation of TDSE in the p-space, it will be free from boundary reflection and the complete information will be

retained. Although it has such great advantage, it is difficult to obtain accurate results due to a singularity in the P-space Coulomb kernel. Recently developed P-space TDSE uses Landé subtraction method to remove the singularity in the Coulomb kernel [43]. However, a larger upper bound  $p_{max}$  is still needed due to the typical usage of Landé subtraction method requiring a larger upper bound  $p_{max}$  for accuracy. This larger upper bound  $p_{max}$  makes the time propagation of P-space TDSE not efficient.

In the first part of this thesis, we modify the Landé subtraction method to be applicable in a smaller  $p_{max}$ , so called "Landé subtraction method with finite integration limits". Together with split-operator method in energy representation, we develop an accurate as well as efficient scheme to perform P-space TDSE [44]. In addition, we also apply the Landé subtraction method with finite integration limits to generalize the Lewenstein model by taking scattering process into account. Next, we apply the developed scheme to the study of strong-field ionization of a lithium atom [45].

Lithium atom is the third element in the periodic table. It has three electrons. The simplest atoms, hydrogen and helium, have been studied for long time, but the double ionization and correlation effect of the two electrons of a helium atom can be carefully studied only recently [46, 47, 48] due to the advance of GPU parallel calculation. And, the dynamics of a lithium atom under strong laser field become the next challenge and start to attract attention [49, 50, 51]. A recent paper reported experimental results together with numerical TDSE calculations on the strong-field ionization of a lithium atom [51]. Two new techniques are used in the experiment: (1) experiment was performed in a magnetic-optical trap (MOT) and the thermal effect is small. (2) the reaction microscope technique was used to measure photoelectron spectra and the resolution is improved to  $\sim$ meV. In the experiment, a laser pulse with full width at half maximum (FWHM) 30fs wavelength 785 nm and peak intensity in  $10^{11} \sim 10^{14}$  were used. The classical estimation by DC field, the laser intensity for OBI is  $I_P^4/16Z^2$ , where  $Z$  is atomic number and  $I_P$  is ionization potential. The OBI intensity for Li is  $3.4 \times 10^{14} W/cm^2$  hence  $\gamma = 3.7$  for wavelength 785 nm used in the experiment. This is in the MPI regime not in the TI regime as inert gas atoms. Therefore, with the lithium target under the laser parameters used in the experiment, MPI, OBI and TI regimes are all covered.

The two-dimensional momentum distributions and the photoelectron spectra were shown in the experimental paper. At lower intensity, the photoelectron spectra is originated simply through nonresonant multiphoton ionization (NRMPI). At a little higher intensity, the intermediate bound states might be populated largely due to ac-Stark shift during pulse time and lead to a dynamical resonant multiphoton ionization (DRMPI) [10]. Complex peaks thus appear. For intensity higher than  $8 \times 10^{12} W/cm^2$ , fanlike structure appears. The long-range Coulomb interaction between the electron and its parent ion, and

ponderomotive shift induced subpeaks explain this structure [52, 53, 54]. We also observed electron is distributed in the direction perpendicular to the polarization axis in the higher laser intensity regime. We perform calculations to examine the above mechanisms further.



# Chapter 2

## Methods

In the section 2.1, the scheme of the split-operator method in the energy representation that we employ to solve the P-space time-dependent Schrödinger equation (P-space TDSE) will be introduced. The most troublesome issue in this scheme is that there exist a singularity in the P-space Coulomb potential. In the section 2.2, we will introduce Landé subtraction method which is a useful technique to remove such singularity. However, typical usage of this technique needs a larger upper bound in momentum  $p_{max}$  to guarantee the accuracy. This limitation make the application to the P-space TDSE not efficient. We modify the Landé subtraction method to be applicable to a smaller momentum upper bound. Accuracy as well as efficiency in time propagation are thus improved. Results of P-space TDSE will be presented in the section 2.3. In the section 2.4, we first introduce two versions of strong field approximation which are very useful theoretical models to investigate the laser-atoms interaction under strong field. One is Keldysh-Faisal-Reiss (KFR) theory and the other is Lewenstein model. Then, we generalize the Lewenstein model to include scattering process by using Landé subtraction method with finite integration limits introduced in the section 2.2.

## 2.1 Time-dependent Schrödinger equation in momentum space

### (P-space TDSE)

The R-space TDSE of an atom interacting with laser field in the velocity gauge is given by

$$i\frac{\partial}{\partial t}\Psi(\mathbf{r}, t) = [H_0 + H_i(t)]\Psi(\mathbf{r}, t) \quad (2.1)$$

$$H_0 = \frac{p^2}{2} + U(r) \quad (2.2)$$

$$H_i(t) = \mathbf{A}(t) \cdot \mathbf{p} \quad (2.3)$$

$$\mathbf{A}(t) = -\int_{-\infty}^t \mathbf{E}(t) dt \quad (2.4)$$

where  $H_0$  is atomic Hamiltonian,  $U(r)$  is the atomic potential which only the motion of the outer most electron is considered (called single-active-electron approximation),  $H_i$  is the laser-electron interaction in the velocity gauge and dipole approximation [Appendix], and  $\mathbf{E}(t)$  and  $\mathbf{A}(t)$  are electric field and its corresponding vector potential of the laser field. Atomic units (a.u.) are used throughout this thesis unless indicated otherwise. The P-space TDSE can be obtained by Fourier transformation [57, 58]:

$$i\frac{\partial}{\partial t}\Psi(\mathbf{p}, t) = [H_0 + H_i(t)]\Psi(\mathbf{p}, t) \quad (2.5)$$

$$H_0\Psi(\mathbf{p}, t) = \frac{p^2}{2}\Psi(\mathbf{p}, t) + \int V(\mathbf{p}, \mathbf{q})\Psi(\mathbf{q}, t)d\mathbf{q} \quad (2.6)$$

$$H_i(t) = \mathbf{A}(t) \cdot \mathbf{p} \quad (2.7)$$

where

$$\Psi(\mathbf{p}, t) = \frac{1}{(2\pi)^{3/2}} \int \Psi(\mathbf{r}, t) \exp(-i\mathbf{p} \cdot \mathbf{r}) d\mathbf{r} \quad (2.8)$$

$$V(\mathbf{p}, \mathbf{q}) = \frac{1}{(2\pi)^3} \int U(r) \exp[i(\mathbf{q} - \mathbf{p}) \cdot \mathbf{r}] d\mathbf{r} \quad (2.9)$$

We use second-order split-operator method to approach the time propagation of wave function.

$$\Psi(\mathbf{p}, t + \Delta t) \approx e^{-iH_0\Delta t/2} e^{-iH_i(t+\Delta t/2)\Delta t} e^{-iH_0\Delta t/2} \Psi(\mathbf{p}, t) + O(\Delta t^3) \quad (2.10)$$



The time propagation of the wave function from  $t$  to  $t+\Delta t$  can be divide into three steps:

(i) free propagate for a half-time step  $\Delta t/2$

$$\Psi_1(\mathbf{p}, t + \Delta t/2) \equiv e^{-iH_0\Delta t/2}\Psi(\mathbf{p}, t) \quad (2.11)$$

(ii) propagate under the influence of the laser field

$$\Psi_2(\mathbf{p}, t + \Delta t/2) \equiv e^{-iH_i(t+\Delta t/2)\Delta t}\Psi_1(\mathbf{p}, t + \Delta t/2) \quad (2.12)$$

(iii) free propagate for another half-time step  $\Delta t/2$

$$\Psi(\mathbf{p}, t + \Delta t) \equiv e^{-iH_0\Delta t/2}\Psi_2(\mathbf{p}, t + \Delta t/2) \quad (2.13)$$

In step (i), we first expand  $\Psi(\mathbf{p}, t)$  and  $V(p, p')$  in spherical harmonics  $Y_{lm}(\theta, \phi)$ . In the following, we will only present linear polarized case, and can be generalized to any polarization easily under the same framework. For a linear polarized light, the system is azimuthal symmetric by assigning the polarization direction as the  $z$  axis. Therefore, only  $m = 0$  components will be involved.

$$\Psi(\mathbf{p}, t) = \sum_{l=0}^{l_{max}} g_l(p, t) Y_{l0}(\theta, \phi) \quad (2.14)$$

$$V(\mathbf{p}, \mathbf{q}) = \frac{1}{pq} \sum_{l=0}^{l_{max}} v_l(p, q) Y_{l0}(\theta, \phi) Y_{l0}^*(\theta', \phi') \quad (2.15)$$

where  $l_{max}$  is the maximum number of partial wave and  $v_l(p, q)$  will be expressed later in Eq. (2.37). Then, Eq. (2.11) can be rewritten as:

$$\exp(-iH_0\Delta t/2)\Psi(p_i, \theta_j, t) = \sum_{l=0}^{l_{max}} [\exp(-iH_0^l\Delta t/2)g_l(p_i, t)]Y_{l0}(\cos\theta_j) \quad (2.16)$$

where

$$H_0^l\Psi(p, t) = \frac{p^2}{2} + \int v_l(p, q)\Psi(q, t)q^2dq \quad (2.17)$$

is the radial part of the atomic Hamiltonian. Next, we represent the time evolution operator  $S^l \equiv \exp(-iH_0^l\Delta t/2)$  in complete eigensets  $\chi_{kl}(p)$  of the atomic Hamiltonian  $H_0^l$ . This scheme is the so called split-operator method in the energy representation [34]. And,  $\chi_{kl}(p)$  satisfies the following eigenvalue equation:

$$H_0^l\chi_{kl}(p) = \frac{p^2}{2}\chi_{kl}(p) + \int v_l(p, q)\chi_{kl}(q)q^2dq = \varepsilon_{kl}\chi_{kl}(p) \quad (2.18)$$

where  $\varepsilon_{kl}$  is the eigen energy corresponding to  $\chi_{kl}(p)$ . The time evolution of the radial part of Eq. (2.16) can thus be expressed as:

$$[\exp(-iH_0^l\Delta t/2)g_l(p)]_i = \sum_{j=1}^N S_{ij}^l g_l(p_j) \equiv g_l^{(1)}(p_i) \quad (2.19)$$

where

$$S_{ij}^l = \sum_k \chi_{kl}(p_i) \chi_{kl}(p_j) \exp(-i\varepsilon_{kl}\Delta t/2) \quad (2.20)$$

Combining with angular part we get  $\Psi_1(\mathbf{p}, t)$ :

$$\Psi_1(\mathbf{p}, t + \Delta t/2) = \sum_{l=0}^{l_{max}} g_l^{(1)}(p, t) Y_{l0}(\theta, \phi) \quad (2.21)$$

In step (ii), see Eq. (2.12),  $H_i(t + \Delta t/2) = A(t + \Delta t/2)p \cos \theta$  for linear polarized light. Rather than coupling in  $p$ -subspace for each independent  $l$  through the convolution integration of the atomic potential in step (i), the  $\cos \theta$  in  $H_i$  couple the  $l$ -subspace for each  $p$  independently here. We change the character of  $p$  and  $l$  and rewriting Eq. (2.21) as follow [43]:

$$\Psi_1(\mathbf{p}, t + \Delta t/2) = \sum_{l=0}^{l_{max}} g_p^{(1)}(l, t) Y_{l0}(\theta, \phi) \quad (2.22)$$

And, we represent the time evolution operator  $\exp[-iH_i(t + \Delta t/2)\Delta t]$  in the complete sets  $\chi_{\ell p}^{(1)}(l)$  of the operator  $\hat{K} = \cos \theta$  in the  $\{Y_{l0}(\theta, \phi)\}$  basis which satisfies

$$\hat{K} \chi_{\ell p}^{(1)}(l) = \lambda_{\ell p} \chi_{\ell p}^{(1)}(l) \quad (2.23)$$

where  $\lambda_{\ell p}$  is the eigenvalue corresponding to  $\chi_{kl}^{(1)}(p)$ . Then, together with Eq. (2.22), Eq. (2.12) can be rewritten as:

$$\Psi_2(\mathbf{p}, t + \Delta t/2) = \sum_{l=0}^{l_{max}} \sum_{j=1}^{l_{max}} S_{ij}^p g_p^{(1)}(l_j, t) Y_{l0}(\theta, \phi) \quad (2.24)$$

where

$$S_{ij}^p = \sum_{\ell} \chi_{\ell p}^{(1)}(l_i) \chi_{\ell p}^{(1)}(l_j) \exp(-iA(t + \Delta t/2)p \lambda_{\ell p} \Delta t) \quad (2.25)$$

Step (iii) is just the same as step (i). After repeating step (i) again, the wave function  $\Psi(\mathbf{p}, t + \Delta t)$  is obtained.

After propagating to the end of the laser field at  $t_f$ , we get a final time wave function  $\Psi(t_f)$ . To extract the information of the ionized electron, we introduce a continuous state projection operator:

$$\hat{P}_C = \sum_{E_i \geq 0} |\chi_i\rangle \langle \chi_i| \quad (2.26)$$

which is a summation of the outer product of eigenstates with positive eigen energy. Then, we can isolate the continuous part  $\Psi_C$  by operating  $\hat{P}_C$  to the final time wave function  $\Psi(t_f)$ .

$$\Psi_C = \hat{P}_C \Psi(t_f) \quad (2.27)$$

The momentum differential probability  $P$  distribution of the an ionized electron of energy  $E = p^2/2$  in the direction  $\hat{\mathbf{p}}$  is given by

$$\frac{\partial^3 P}{\partial^3 \mathbf{p}} = |\Psi_C|^2 \quad (2.28)$$

For a linear polarized light, the system is symmetric about the polarization axis. Two-dimensional momentum distribution can be obtained by integrated over the azimuthal angle  $\phi$  about the polarization axis.

$$\frac{\partial^2 P}{\partial E \partial \theta} = \frac{\partial^3 P}{\partial^3 \mathbf{p}} 2\pi p \sin \theta \quad (2.29)$$

or

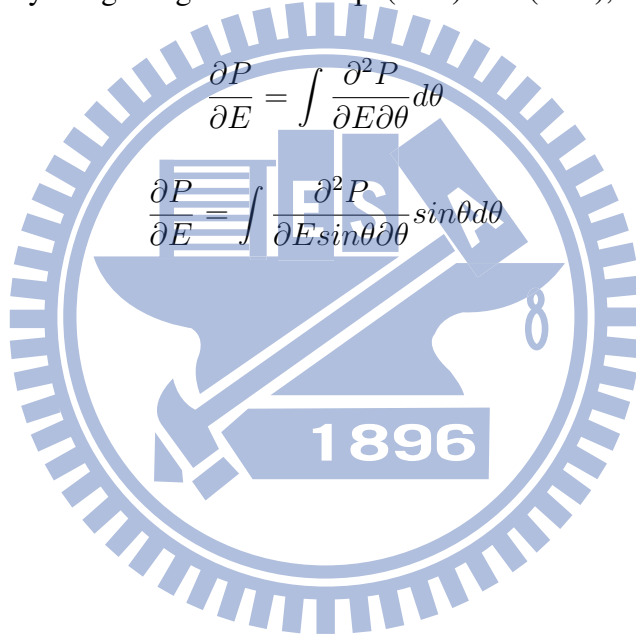
$$\frac{\partial^2 P}{\partial E \sin \theta \partial \theta} = \frac{\partial^3 P}{\partial^3 \mathbf{p}} 2\pi p \quad (2.30)$$

where  $\theta$  is the angle between the polarization axis and the direction of the ionized photoelectron. The former form usually use to emphasize multiphoton ionization pattern [59] while latter one usually use to emphasize the electron distribution along the polarization direction [39, 43]. By integrating over  $\theta$  in Eq. (2.29) and (2.30), we obtain the photoelectron spectra.

$$\frac{\partial P}{\partial E} = \int \frac{\partial^2 P}{\partial E \partial \theta} d\theta \quad (2.31)$$

or

$$\frac{\partial P}{\partial E} = \int \frac{\partial^2 P}{\partial E \sin \theta \partial \theta} \sin \theta d\theta \quad (2.32)$$



## 2.2 Landé subtraction method with finite integration limits

Since we represent the time evolution operator  $S^l \equiv \exp(-iH_0^l \Delta t/2)$  in complete eigensets of atomic Hamiltonian  $H_0^l$ , solving the eigenvalue equation Eq. (2.18) is the central part of the P-space TDSE. Before proceeding, let's examine the atomic potential first. In the single-active-electron approximation, only the motion of the outer most electron is considered. The interaction between this electron and other inner shell electrons and atomic core can be modeled as a model potential [14, 60, 61]. The form of a model potential is not unique. We list one for example [61]:

$$V(r) = -\frac{1}{r} - \frac{a_1 e^{-a_2 r} + a_3 r e^{-a_4 r} + a_5 e^{-a_6 r}}{r} \quad (2.33)$$

When  $r \rightarrow \infty$ ,  $V(r) \rightarrow -1/r$  which is the long-range Coulomb potential between the outer most electron and the ion core. The second short-range potential term account for the screened effect caused by other inner shell electrons where  $a_i$ 's are variation parameters to be optimized by fitting the energy levels from experiment data. This can be done by, for example, density functional calculations. Fourier transformation of this model potential is

$$V(k) = -\frac{1}{2\pi^2 k^2} - \frac{1}{2\pi^2} \left\{ \frac{a_1^2}{a_2^2 + k^2} + \frac{2a_3 a_4}{a_4^2 + k^2} + \frac{a_5^2}{a_6^2 + k^2} \right\} \quad (2.34)$$

where  $k = |\mathbf{p} - \mathbf{q}|$ . Except the first long-range Coulomb potential term have a singularity at  $k = 0$ , others are well-behaved functions in the p-space and are easy to handle. The singularity in long-range Coulomb potential make it difficult to calculate eigenstates as well as eigenvalues accurately. To remove this singularity, Landé subtraction technique has been proposed and the potential part of Eq. (2.18) is rewritten as [55]:

$$\begin{aligned} & \int v_l(p, q) \psi_l(q, t) q^2 dq \\ &= S_l \psi_l(p, t) + \int v_l(p, q) \left[ \psi(q, t) q^2 - \frac{\psi(p, t)}{P_l(z)} p^2 \right] dq \end{aligned} \quad (2.35)$$

where  $z = (p^2 + q^2)/2pq$ ,  $P_l(z)$  is the Legendre polynomial,  $S_l$  is defined as:

$$S_l \equiv p^2 \int \frac{v_l(p, q)}{P_l(z)} dq \quad (2.36)$$

,and  $v_l(p, q)$  is the expansion of p-space Coulomb potential  $(-1/2\pi^2 k^2)$  in  $\{Y_{lm}(\theta, \phi)\}$  basis, see Eq. (2.15), and has the following form:

$$v_l(p, q) = -\frac{1}{\pi pq} Q_l\left(\frac{p^2 + q^2}{2pq}\right) \quad (2.37)$$

$Q_l$  is Legendre function of the second kind and is defined as:

$$Q_l(z) = \frac{1}{2} \int_{-1}^1 \frac{1}{z-x} P_l(x) dx \quad (2.38)$$

when  $p = q$ , hence  $z = 1$ ,  $v_l(p, q)$  diverge because  $Q_l(z)$  is divergent.

In Eq. (2.35), we just subtract the potential part of Eq. (2.18) by  $p^2 \int v_l(p, q) \frac{\psi(p, t)}{P_l(z)} dq$  and add it back. By this trick, the terms in the square bracket tend to zero faster than the Coulomb potential  $v_l(p, q)$  tends to infinity when  $q \rightarrow p$  and singularity is thus removed. Hence we can redefine  $v_l(p, q)$  for convenience [43]

$$v_l(p, q) = \begin{cases} 0 & p = q \\ V_l(p, q) & p \neq q \end{cases} \quad (2.39)$$

Then, the eigenvalue equation Eq. (2.18) can be rewritten as:

$$\left[ \frac{p^2}{2} + S_l - q_l(p) \right] \chi_{kl}(p) + \int V_l(p, q) \chi_{kl}(q) q^2 dq = \varepsilon_{kl} \chi_{kl}(p) \quad (2.40)$$

where

$$q_l(p) = p^2 \int \frac{V_l(p, q)}{P_l(z)} dq \quad (2.41)$$

Now, we need to calculate  $S_l$  and  $q_l(p)$  in the Eq. (2.40). We rewrite  $S_l$  as following:

$$S_l = p^2 \int \frac{v_l(p, q)}{P_l(z)} dq = \frac{-p}{\pi} \int \frac{Q_l(z)}{q P_l(z)} dq = -p J_l(p) \quad (2.42)$$

where  $J_l(p)$  is defined as

$$J_l(p) \equiv \frac{1}{\pi} \int \frac{Q_l(z)}{q P_l(z)} dq \quad (2.43)$$

and the Legendre function of the second kind can be expressed alternatively as [62]

$$Q_l(z) = \frac{1}{2} P_l(z) \ln \frac{z+1}{z-1} - W_{l-1}(z) \quad (2.44)$$

where

$$W_{l-1}(z) = \sum_{k=1}^l \frac{1}{k} P_{k-1}(z) P_{l-k}(z) \quad (2.45)$$

Finally,  $J_l(p)$  has the form

$$J_l(p) = \frac{1}{2\pi} \int \ln \frac{z+1}{z-1} \frac{dq}{q} - \frac{1}{\pi} \int \frac{W_{l-1}(z)}{P_l(z)} \frac{dq}{q} \quad (2.46)$$

We should integral the two terms on the right hand side of Eq. (2.46) from 0 to  $\infty$  and these two terms can be calculated analytically. The first term is

$$\frac{1}{2\pi} \int_0^\infty \ln \frac{z+1}{z-1} \frac{dq}{q} = \frac{\pi}{2} \quad (2.47)$$

$l$	$I_l$	$l$	$I_l$
0	0	10	1.487904713975699
1	1	11	1.495107943133761
2	1.224744871391589	12	1.501159656551487
3	1.322854905602328	13	1.506315483232877
4	1.377702237793946	14	1.510760615105643
5	1.412705039729489	15	1.514632500321632
6	1.436975208969198	16	1.518035295340011
7	1.454789864925959	17	1.521049367745399
8	1.468421032379340	18	1.523737720224722
9	1.479186912585977	19	1.526150439737141

Table 2.1: Numerical values of  $I_l$  for  $l=0-19$ . [56].

We neglect the detail calculation of the second term and just define its as  $I_l$ , so

$$J_l(p) = \frac{\pi}{2} I_l \quad (2.48)$$

Numerical values of  $I_l$  for  $l = 0 - 19$  are listed in Table 1 [56]. However, in the numerical calculation, we can only set a finite upper bound  $p_{max}$  rather than  $\infty$ . Since  $J_l(p)$  is obtained by integrating momentum  $q$  from 0 to  $\infty$ , setting a larger upper bound  $p_{max}$  as well as a large number of grid points for obtaining accurate eigenstates and eigenvalues is expected. As a result, the calculation is inefficient.

This problem can be cured by setting the integration upper bound of  $J_l(p)$  to a finite value  $p_{max}$ . We denote the modified  $J_l$  by  $J_l^{finite}(p)$ . That is

$$J_l^{finite}(p) = \frac{1}{2\pi} \int_0^{p_{max}} \ln \frac{z+1}{z-1} \frac{dq}{q} - \frac{1}{\pi} \int_0^{p_{max}} \frac{W_{l-1}(z)}{P_l(z)} \frac{dq}{q} \quad (2.49)$$

and the first term becomes

$$\frac{1}{2\pi} \int_0^{p_{max}} \ln \frac{z+1}{z-1} \frac{dq}{q} = \frac{\pi}{2} - \frac{2}{\pi} \left[ s + \frac{s^3}{3^2} + \frac{s^5}{5^2} + \frac{s^7}{7^2} + \dots \right] \quad (2.50)$$

where  $s = p/p_{max}$ . The second term of  $J_l^{finite}(p)$  can be calculated numerically. Together with the numerical integration of  $q_l(p)$  from 0 to  $p_{max}$ , the eigenvalue equation Eq. (2.40) is ready to solve [63].

We map the P-space domain  $p \in [0, p_{max}]$  to a new domain  $x \in [-1, 1]$  by the following mapping function:

$$p(x) = L \frac{1+x}{1-x+x_m} \quad (2.51)$$

where  $L$  is mapping parameter and  $x_m = 2L/p_{max}$ . The grid points are denser at small  $p$  for smaller  $L$ .  $x$  is discretized by using Gauss-Lobatto quadrature where the  $N$  grid points  $\{x_i\}$  are the roots of the derivative of Legendre polynomial  $P'_{N+1}(x)$  [64].

<i>State</i> (nl)	<i>E(nl) – exact</i>		$\Delta\Phi$	
	Present	Ordinary	Present	Ordinary
1s	1.76(-6)	-6.45(-3)	6.90(-8)	2.45(-4)
2s	2.75(-7)	-1.61(-3)	6.88(-8)	4.25(-4)
3s	1.24(-7)	7.16(-4)	6.88(-8)	6.17(-4)
2p	-1.56(-10)	-4.14(-8)	1.01(-10)	1.34(-8)
3p	-8.75(-10)	1.83(-8)	6.46(-10)	1.84(-8)
3d	2.38(-10)	2.38(-10)	4.21(-10)	4.22(-10)

Table 2.2: Comparison of eigenvalues and wave functions of a hydrogen atom between "Present" Landé subtraction method method with finite limits and the "Ordinary" Landé subtraction method.  $[E(nl)-exact]$  is the deviation of energy levels for the first few low-lying states.  $\Delta\Phi$  is the root-mean-square deviation of the wave function. 2048 grid points and  $p_{max} = 100$  a.u. are used.  $1.76(-6) \equiv 1.76 \times 10^{-6}$  [44].

<i>State</i> (nl)	<i>E(nl) – exact</i>		$\Delta\Phi$	
	Present	Ordinary	Present	Ordinary
1s	7.77(-8)	-3.18(-4)	5.99(-10)	1.22(-5)
2s	6.55(-8)	-7.96(-5)	1.01(-9)	2.11(-5)
3s	6.25(-8)	-3.53(-5)	1.41(-9)	3.07(-5)
2p	-1.78(-10)	-4.95(-10)	4.39(-9)	1.90(-10)
3p	-9.45(-10)	-1.06(-9)	6.85(-8)	7.69(-10)
3d	3.86(-10)	2.70(-10)	7.66(-8)	5.58(-10)

Table 2.3: The same as Table 2.3, but 2048 grid points and  $p_{max} = 2000$  a.u. are used [44].

In the Table 2.2 and 2.3, we present the energy deviation and root-mean-square deviation of the radial wave functions between our numerical results and exact ones of a hydrogen atom. Root-mean-square deviation of the wave functions is defined as:

$$\Delta\Phi = \sqrt{\frac{1}{N} \int p^2 dp |\Phi(p) - \Phi_{exact}(p)|^2} \quad (2.52)$$

$\Phi_{exact}$  is the exact wave function of a hydrogen atom in the P-space. and first few low-lying states are listed in the following [57, 58]:

$$F_{10}(p) = \frac{2^{5/2}}{\pi} \frac{1}{(p^2 + 1)^2} \quad (2.53)$$

$$F_{20}(p) = \frac{32}{\sqrt{\pi}} \frac{4p^2 - 1}{(4p^2 + 1)^3} \quad (2.54)$$

$$F_{21}(p) = \frac{128}{\sqrt{3\pi}} \frac{p}{(4p^2 + 1)^3} \quad (2.55)$$

”Ordinary” means the results of using typical Landé subtraction method while ”Present” means the results of using Landé subtraction method with finite integration limits. In Table 2.2, 2048 grid points and  $p_{max} = 100$  a.u. are used. In Table 2.3, 2048 grid points and  $p_{max} = 2000$  a.u. are used. As mentioned above, typical Landé subtraction method needs a larger  $p_{max}$  to ensure the accuracy. Therefore, the ”Ordinary” results for  $p_{max} = 2000$  a.u. are more accurate than those for  $p_{max} = 100$  a.u.. We can find the ”Present” results improve the accuracy to several order than ”Ordinary” results at  $p_{max} = 2000$  a.u. as well as  $p_{max} = 100$  a.u.. The results are more accurate at larger  $p_{max}$  for both methods, especially for the s states. This is because P-space radial wave function tends to  $1/p^{l+4}$  when  $p \rightarrow \infty$ . So, s states ( $l = 0$ ) are the most diffusive states, a larger  $p_{max}$  is needed to reach higher accuracy. The improvement of the results to an acceptable accuracy at small  $p_{max}$  by the ”Present” method will make the time propagation of TDSE more efficient, as we will see in the next section.

In Fig. 2.1, we compare the numerical wave function for the ”Present” Landé subtraction method method with finite limits to exact ones for the first few low-lying states of a hydrogen atom. 2048 grid points are used and left column for  $p_{max} = 100$  a.u. while right column for  $p_{max} = 2000$  a.u.



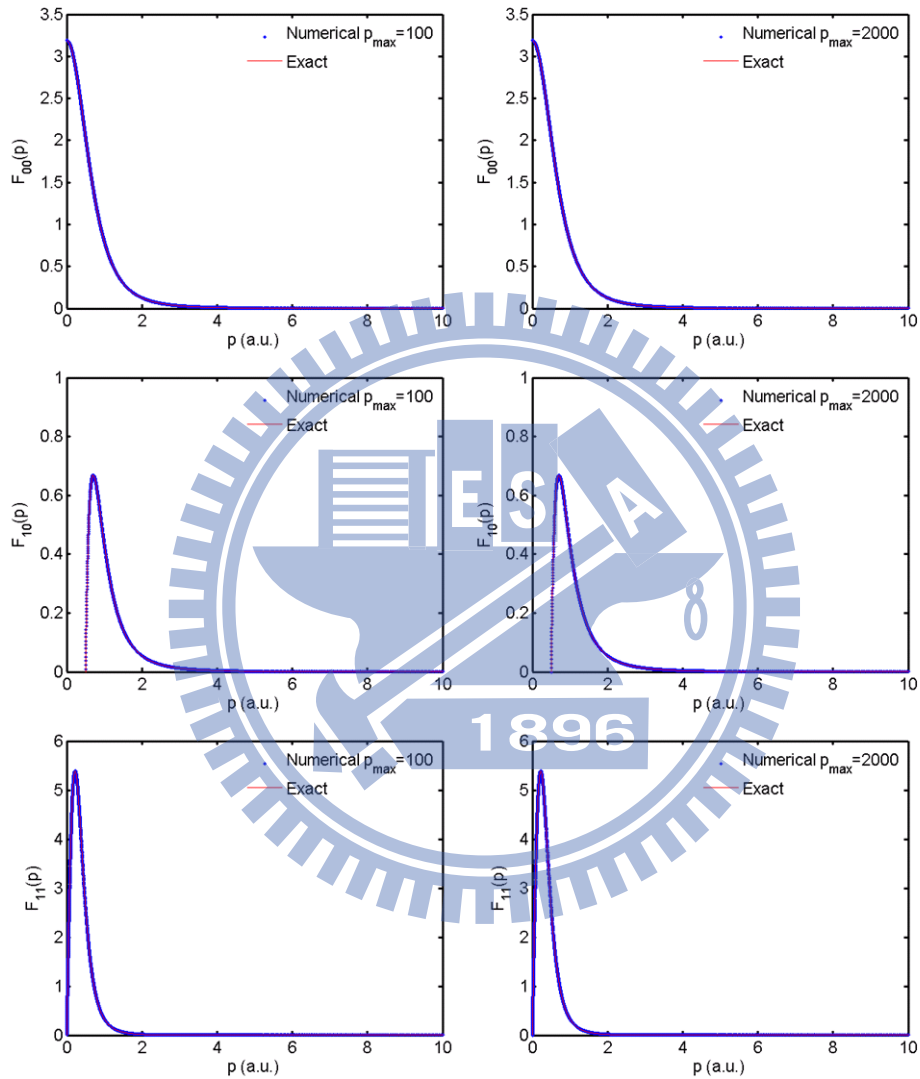


Figure 2.1: Comparison of the numerical wave functions of "Present" Landé subtraction method method with finite limits with the exact ones for the first few low-lying states of a hydrogen atom. 2048 grid points are used and left column for  $p_{max} = 100$  a.u. while right column for  $p_{max} = 2000$  a.u..

## 2.3 Results of P-space TDSE

In this section, we will present our P-space TDSE results and the emphasis will be put on the convergent test and calibration. The physics underlying laser-atom interaction under strong field will be discussed on the subject of the strong-field ionization of a lithium atom in the next chapter.

### 2.3.1 Linear polarization case

The linear polarized electric field  $\mathbf{E}(t)$  of a laser pulse along the  $z$  axis can be described by

$$\mathbf{E}(t) = E_0 f(t) \cos(\omega t + \phi) \hat{z} \quad (2.56)$$

where  $E_0$  is the peak electric field,  $\omega$  is the carrier frequency,  $\phi$  is the carrier-envelope phase (CEP). We choose a cosine-square pulse which the envelope function is

$$f(t) = \cos^2\left(\frac{\pi t}{T}\right) \quad (2.57)$$

for the time interval  $(-T/2, T/2)$  and zero elsewhere.  $T$  is the full width of the laser pulse, which is 2.75 times of full width at half maximum (FWHM). Vector potential of the laser field can be obtained by

$$\mathbf{A}(t) = -\int_{-\infty}^t \mathbf{E}(t) dt \quad (2.58)$$

In Fig. 2.2, we present  $\mathbf{E}(t)$  and  $\mathbf{A}(t)$  of a five-cycle pulse. Amplitudes are both normalized to unity.

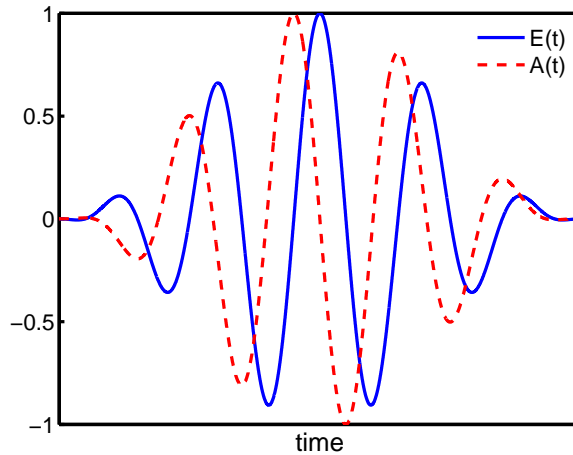


Figure 2.2: Electric field  $\mathbf{E}(t)$  and vector potential  $\mathbf{A}(t)$  of a five-cycles pulse. Amplitudes are both normalized to unity.

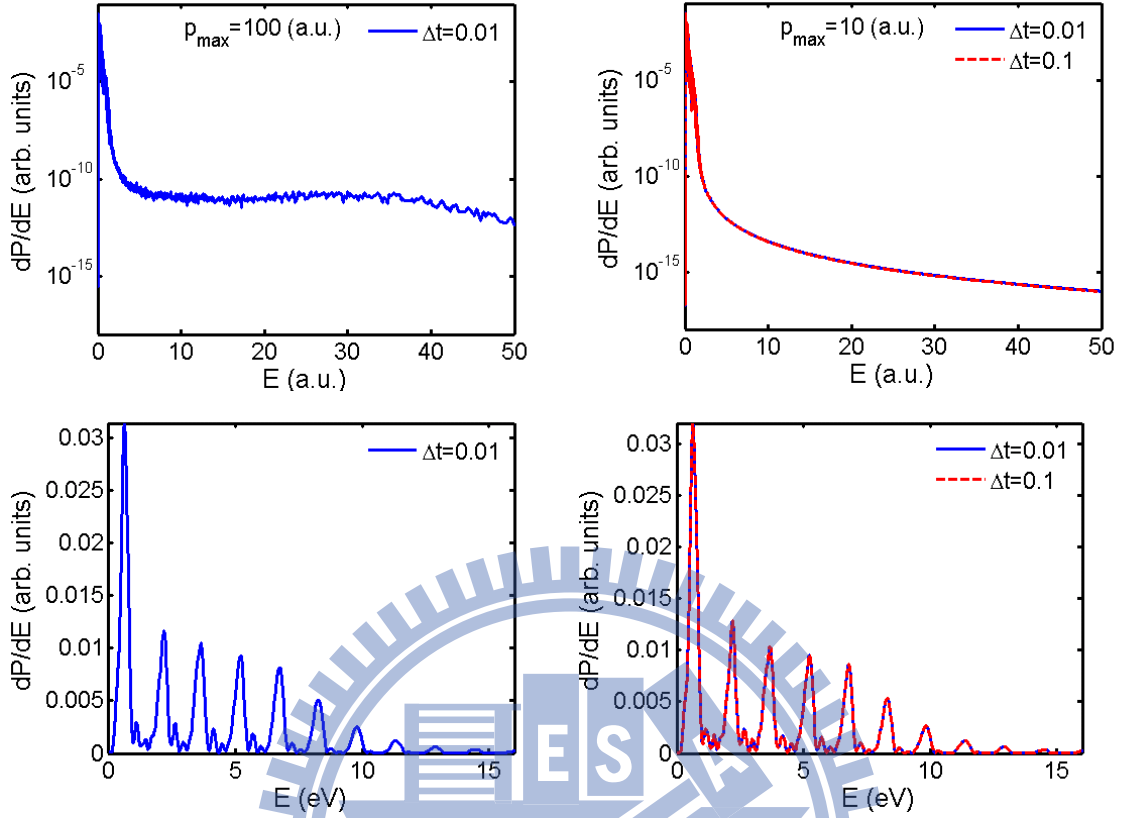


Figure 2.3: Comparison of the photoelectron spectra for  $p_{max} = 100$  (left column) and  $p_{max} = 10$  (right column) of a hydrogen atom with a linear polarized laser pulse with  $T=20$  cycles, wavelength 800 nm, peak intensity  $5 \times 10^{13} W/cm^2$ , and  $\phi = 0$ . The up row is in logarithm scale while the bottom row are in linear scale.

We consider a hydrogen atom under the laser pulse with  $T=20$  cycles, wavelength 800 nm, peak intensity  $5 \times 10^{13} W/cm^2$ , and  $\phi = 0$ . In the calculation, we use 2048 grid points,  $l_{max} = 14$ . In Fig. 2.3, we compare the P-space TDSE results for  $p_{max} = 100$  a.u. (left column) and 10 a.u. (right column). The x-axis is plotted to 50 (a.u.) [1355 (e.v.)] in the up row while that is only plotted to 15 (e.v.) in the bottom row. At lower energy (bottom row), results are consistent between two different  $p_{max}$ . However, we find that photoelectron spectra are not convergent yet after about 5 (a.u.) for the case of  $p_{max} = 100$  a.u. and time step  $\Delta t = 0.01$  a.u. (left top), since the probability of ionized electron should be decay gradually toward high energy. But, for  $p_{max} = 10$  a.u., the photoelectron spectra is convergent very well even  $\Delta t = 0.1$  a.u. (right top). The case of  $\Delta t = 0.1$  a.u. only take 1/10 computation time than that of  $\Delta t = 0.01$  a.u.. As a result, the the Landé subtraction method with finite integration limits improves the accuracy of the eigensets for a small  $p_{max}$  and thus make the P-space TDSE more efficiency.

In Fig. 2.4, we present the two dimension momentum distribution of the ionized electron of the same system. Left sub-figure is from Ref. [43] and right sub-figure is our

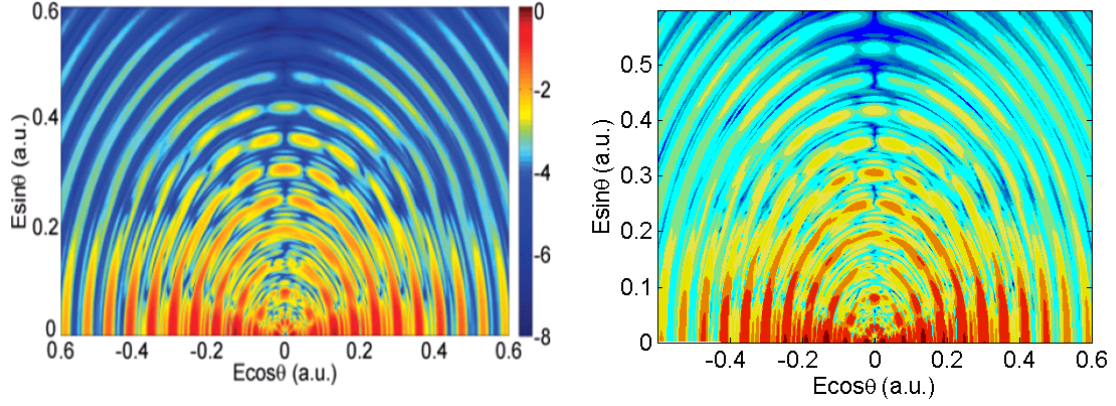


Figure 2.4: Comparison of the two-dimensional momentum distribution of the same system as Fig. 2.3. Left sub-figure is from Ref. [43] and Right sub-figure is our result.

results. Two results are consistent. We can find distinct ATI rings clearly.

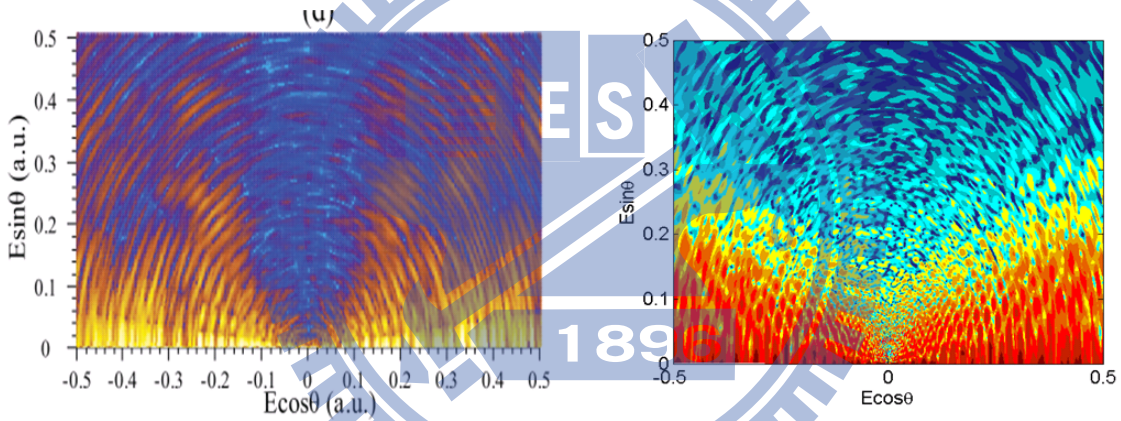


Figure 2.5: Comparison of the two-dimensional momentum distribution of a hydrogen atom with a linear polarized laser pulse with  $T=10$  cycles, wavelength 2000 nm, peak intensity  $1 \times 10^{14} W/cm^2$ , and  $\phi = 0$ . Left sub-figure is from Ref. [39] and right sub-figure is our result.

As another test, we consider a hydrogen atom under the laser pulse with  $T=10$  cycles, wavelength 2000 nm, peak intensity  $1 \times 10^{14} W/cm^2$ , and  $\phi = 0$ . For a pulse in such mid-infrared regime, the amplitude of free quiver motion of a electron in the laser field  $\alpha = E_0/\omega^2$  become larger. Therefore, a larger boundary box is expected in the R-space TDSE calculation and the computation time increases exponentially. However, there is no such problem in the P-space TDSE. In Fig. 2.5, we present the two dimension momentum distribution of the ionized electron. Left sub-figure is from Ref. [39] and right sub-figure is our results. In the calculation, we use 1024 grid points,  $l_{max} = 40$ ,  $p_{max} = 10$  a.u., and  $\Delta t = 0.05$  a.u. Our result agree with theirs in the polarization direction (x axis) but lack of small node structures in their result. We comment that their angular resolution is not

good enough since only 32 angular grid points are used in their result, but we use 401 angular grid points.

### 2.3.2 Elliptical polarization case

The elliptically polarized vector potential  $\mathbf{A}(t)$  of a laser pulse in the x-y plane is given by

$$\mathbf{A} = A_0 f(t) \begin{pmatrix} \cos(\omega t + \phi) \cos(\epsilon/2) \\ \sin(\omega t + \phi) \sin(\epsilon/2) \\ 0 \end{pmatrix} \quad (2.59)$$

where  $A_0$  is the peak amplitude,  $\omega$  is the carrier frequency,  $\phi$  is the carrier-envelope phase (CEP) and  $\epsilon$  is the light ellipticity [ $\epsilon = \pi/2$  (0) for circular polarization (linear polarization along  $\hat{x}$ )]. We choose a cosine-square pulse the same as Eq. (2.53).

We consider a hydrogen atom under the laser pulse with  $T=3$  cycles, wavelength 800 nm, peak intensity  $1.06 \times 10^{14} \text{ W/cm}^2$ ,  $\phi = -\pi/2$ , and  $\epsilon = \pi/2$  (circular polarization). In the calculation, we use 256 grid points,  $l_{max} = 40$ ,  $p_{max} = 100(a.u.)$ , and  $\Delta t = 0.1(a.u.)$ . In Fig. 2.6, we show the two-dimensional momentum distribution of ionized electron in the x-y plane (or  $\theta = 0$  plane). The left sub-figure is from Ref. [65]. Our result agree well with theirs.

For elliptical polarization case, all magnetic quantum number  $m$  will be involved. Given a  $l_{max}$ , the total angular subspace is  $(l_{max} + 1)^2$  which is an order greater than the linear polarized case. Therefore, the calculation is much more expansive than the linear polarization case. In this case, we have used GPU parallel calculation (Tesla), but it still take about 29 hours.

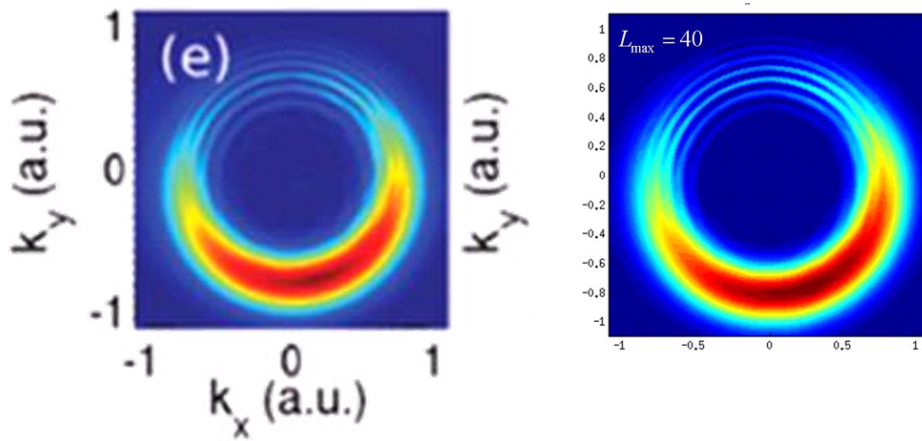


Figure 2.6: Comparison of the two-dimensional momentum distribution in the x-y plane of a hydrogen atom with a circular polarized laser pulse with  $T=3$  cycles, wavelength 800 nm, peak intensity  $1.06 \times 10^{14} \text{ W/cm}^2$ , and  $\phi = -\pi/2$ . Left sub-figure is from Ref. [65] and right sub-figure is our result.



## 2.4 Strong-field Approximation

Two versions of strong-field approximation will be introduced in this section. One is based on S-matrix theory which is named Keldysh-Faisal-Reiss (KFR) theory [8, 32, 33]. The other is based on an ansatz wave function which only the atomic ground state and continuous states are considered and first proposed by M. Lewenstein et al. [7].

### 2.4.1 Keldysh-Faisal-Reiss (KFR) theory

An exact expression for the probability amplitude of detecting an ionized electron with momentum  $\mathbf{p}$  can be written as [59, 66]:

$$f(\mathbf{p}) = -i \int_{-\infty}^{\infty} \langle \Psi_{\mathbf{p}} | U(t, t') H_i(t') | \Psi_0(t') \rangle \quad (2.60)$$

where  $U(t, t')$  is the time-evolution operator corresponding to total Hamiltonian  $H(t) = H_0 + H_i(t)$ ,  $H_0 = p^2/2 + V(r)$  is the atomic Hamiltonian,  $H_i = \mathbf{E}(t) \cdot \mathbf{r}$  is the laser-atom interaction in the length gauge, and  $\Psi_{\mathbf{p}}(t)$  and  $\Psi_0(t)$  are exact continuous state with moment  $\mathbf{p}$  and ground state.  $U(t, t')$  can be expansion as following:

$$U(t, t') = U_F(t, t') - i \int_{t'}^t dt'' U_F(t, t'') V U(t'', t') \quad (2.61)$$

where  $U_F(t, t')$  is the time-evolution operator corresponding to Hamiltonian  $H_F$  of a free electron in the laser field, and

$$H_F = \frac{p^2}{2} + \mathbf{r} \cdot \mathbf{E} \quad (2.62)$$

We use length gauge form here. The eigenstates of  $H_F$  can be solved exactly and called the Volkov states [Appendix]:

$$|\chi_{\mathbf{p}}\rangle = |\mathbf{p} + \mathbf{A}(t)\rangle \exp[-iS_{\mathbf{p}}(t)] \quad (2.63)$$

where

$$S_{\mathbf{p}}(t) = \frac{1}{2} \int_{-\infty}^{\infty} dt' [\mathbf{p} + \mathbf{A}(t')]^2 \quad (2.64)$$

and  $|\mathbf{k}\rangle$  is plane wave:

$$\langle \mathbf{r} | \mathbf{k} \rangle = \frac{1}{(2\pi)^{3/2}} \exp(i\mathbf{k} \cdot \mathbf{r}) \quad (2.65)$$

so

$$\begin{aligned} \langle \mathbf{r} | \mathbf{k} + \mathbf{A}(t) \rangle &= \frac{1}{(2\pi)^{3/2}} \exp[i(\mathbf{k} + \mathbf{A}(t)) \cdot \mathbf{r}] \\ &= \frac{1}{(2\pi)^{3/2}} \exp(i\mathbf{A}(t) \cdot \mathbf{r}) \exp(i\mathbf{k} \cdot \mathbf{r}) \end{aligned} \quad (2.66)$$

where  $\exp(i\mathbf{A}(t) \cdot \mathbf{r})$  is gauge factor in the length gauge.  $U_F(t, t')$  can be expanded with the Volkov states:

$$U_F(t, t') = \int d\mathbf{k} |\chi_{\mathbf{k}}(t)\rangle \langle \chi_{\mathbf{k}}(t')| \quad (2.67)$$

The key point of the SFA is to approximate the final exact continue state  $\langle \Psi_{\mathbf{p}}(t) |$  by the Volkov state  $\langle \chi_{\mathbf{p}}(t) |$  where the effect of atomic potential is considered small for an ionized electron in the strong field limit. Then, the ionization amplitude can be expressed as:

$$f = f^{(1)} + f^{(2)} + \dots \quad (2.68)$$

$$f^{(1)} = -i \int_{-\infty}^{\infty} dt \langle \chi_{\mathbf{p}}(t) | H_i(t) | \Psi_0(t) \rangle \quad (2.69)$$

$$f^{(2)} = - \int_{-\infty}^{\infty} dt \int_{-\infty}^{\infty} dt' \int d\mathbf{k} \langle \chi_{\mathbf{p}}(t) | V | \chi_{\mathbf{k}}(t) \rangle \langle \chi_{\mathbf{k}}(t') | H_i(t') | \Psi_0(t') \rangle \quad (2.70)$$

$f^{(1)}$  is the first-order SFA (SFA1) and describe a direct ionization process induced by laser field.  $f^{(2)}$  is the second-order SFA (SFA2), and describe rescattering of an ionized electron by the ion core.

We can find that (i) KRF theory is a two-fold perturbation theory. In writing down the exact expression Eq. (2.60), laser-atom interaction  $H_i$  is served as a perturbation. Then, the total time evolution operator in Eq. (2.60) is expanded in atomic potential  $V(\mathbf{r})$ , Eq. (2.61). This is because in the strong field regime, the laser-atom interaction energy becomes comparable to atomic potential energy. Therefore, one can't just take laser-atom interaction as a perturbation as we usually do in the weak field regime. The physical idea underlying SFA is: For initially bounded electron, laser field is treated as a perturbation. Once the electron is ionized, atomic potential  $V(\mathbf{r})$  become smaller for the distant electron and thus is taken as a perturbation. (ii) After doing the expansion Eq. (2.61) and from Eq. (2.67), (and assuming the expansion is convergent), KRF theory only include the ground state and Volkov states, neglecting all other bound states. (iii) Depletion of the ground state is not consider in this theory.

## 2.4.2 Lewenstein model

Another version of SFA first proposed by M. Lewenstein et al. begins by making the following ansatz [7, 67]:

$$|\Psi(\mathbf{r}, t)\rangle = e^{iI_P t} \left[ a(t)|0\rangle + \int d\mathbf{p} \cdot b(\mathbf{p}, t) |\mathbf{p} + \mathbf{A}(t)\rangle \right] \quad (2.71)$$

where  $I_P$  is ionization potential,  $|0\rangle$  and  $|\mathbf{p} + \mathbf{A}(t)\rangle$  are ground state and continuous states with momentum  $\mathbf{p}$ , similar to Eq. (2.66),  $\mathbf{A}(t)$  is gauge factor, and  $a(t)$  and  $b(\mathbf{p}, t)$  are occupation amplitudes to be determined. In this ansatz, only ground state and continuous states are considered. Further, continue states are approximated by plane wave

$$\langle \mathbf{r} | \mathbf{k} \rangle = \frac{1}{(2\pi)^{3/2}} \exp(i\mathbf{k} \cdot \mathbf{r}) \quad (2.72)$$



and the depletion of the ground state is neglected, which means  $a(t) \approx 1$ . So far, all the approximations are similar to KFR theory. After substituting this ansatz into Schrödinger equation in length gauge:

$$i \frac{\partial}{\partial t} \Psi(r, t) = \frac{p^2}{2} + V(r) + \mathbf{E}(t) \cdot \mathbf{r} \quad (2.73)$$

and multiply  $\langle \mathbf{p}'' + \mathbf{A}(t) |$  from left hand side and integrate, we can obtain differential equation for  $b(\mathbf{p}, t)$ :

$$i \frac{\partial b(\mathbf{p}, t)}{\partial t} = \left[ \frac{(\mathbf{p} + \mathbf{A}(t))^2}{2} + Ip \right] b(\mathbf{p}, t) + \langle \mathbf{p} + \mathbf{A}(t) | H_i(t) | 0 \rangle + \int d\mathbf{p}' b(\mathbf{p}', t) \langle \mathbf{p} | V(r) | \mathbf{p}' \rangle \quad (2.74)$$

In the lowest order approximation of Lewenstein model, scattering term  $\langle \mathbf{p} | V(r) | \mathbf{p}' \rangle$  is neglected, and the differential equation can be integrated to give Eq. (2.69). Therefore, the lowest order approximation of Lewenstein model corresponds to the SFA1 of the KFR theory. Now, we recover scattering term by using the Landé subtraction method with finite integration limits described in the section 2.2. Once the singularity in long range Coulomb potential is removed, the coupled-differential equation (coupling among all  $\mathbf{p}$ s) can be solved using standard ODE solver. How does this result relate to KFR theory? If we expand KFR theory to the Nth-order in equation Eq. (2.61), together with Eq. (2.67) and Eq. (2.68), and assume the result has been convergent. Therefore, the terms after the Nth-order can be neglected. We can find that all these N terms we keep only include ground state and Volkov states (other bound states only exist in  $U(t, t')$  which appears after the Nth-order in KFR theory and has been neglected due to convergent assumption.), just similar to the ansatz wave function proposed in the Lewenstein model Eq. (2.71) which only ground state and Volkov states are considered. So, the result of Lewenstein model with scattering term corresponds to summation of all N order of KFR theory since we didn't do such an expansion as Eq. (2.61). Therefore, the Lewenstein model is a nonperturbative model.

### 2.4.3 Results

In Fig. 2.7, we show the photoelectron spectra of the TDSE as well as two versions of SFA results of hydrogen atom under a laser pulse with 5 cycles, wavelength 800 nm, peak intensity  $1 \times 10^{14} \text{ W/cm}^2$ , and  $\phi = 0$ . Left sub-figure is from Ref. [59] using R-space TDSE and KFR theory, while right sub-figure is our results using P-space TDSE and Lewenstein model. "SFA1" and "SFA2" in the left sub-figure means the first and second-order KFR theory respectively. "SUM" means the summation of "SFA1" and "SFA2". "SFA1" in the right sub-figure means the results of solving Eq. (2.74) of Lewenstein

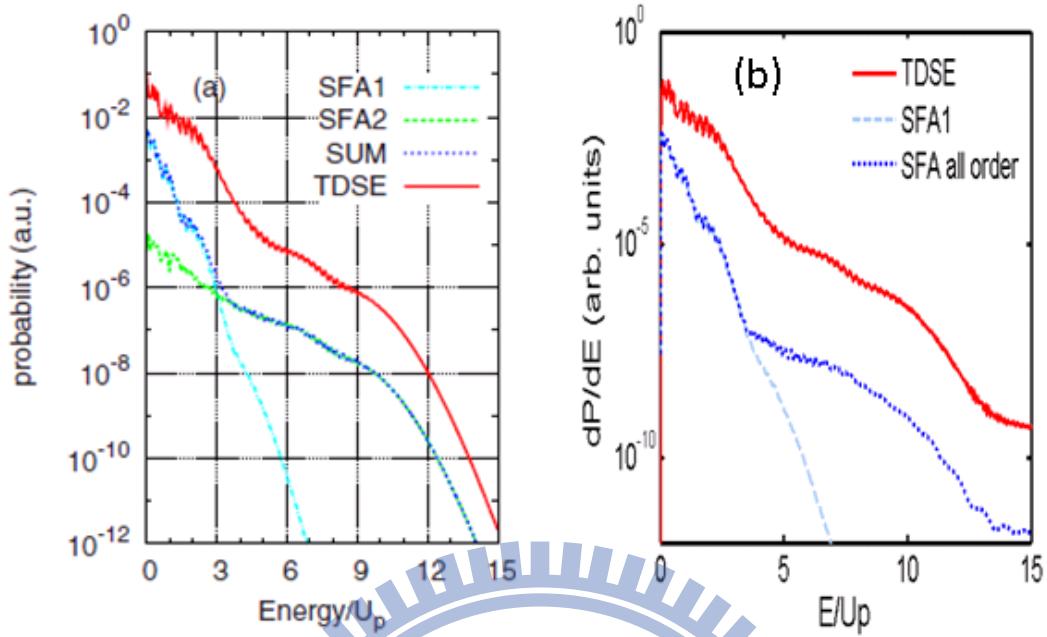


Figure 2.7: Photoelectron spectra of the TDSE as well as two versions of SFA results of a hydrogen atom with a linear polarized laser pulse with 5 cycles, wavelength 800 nm, peak intensity  $1 \times 10^{14} \text{ W/cm}^2$ , and  $\phi = 0$ . Left sub-figure is from Ref. [59] using R-space TDSE and KFR theory, "SFA1" and "SFA2" mean the first and second order of the KFR theory, and "SUM" is the summation of "SFA1" and "SFA2". Right sub-figure is our results using P-space TDSE and Lewenstein model, "SFA1" is the result of Eq. (2.70) without scattering term and corresponding to "SFA1" of the KFR theory, and "SFA all order" contain Coulomb scattering term and corresponding to the summation of all order of the KFR theory.

model without the scattering term  $\langle \mathbf{p} | V(r) | \mathbf{p}' \rangle$  which is just the SFA1 in the KFR theory. "SFA all order" is the result of solving Eq. (2.74). Since we don't do any expansion, this results is corresponding the summation of all order of KFR theory. "SUM" (blue-dotted line) in the left sub-figure is consistent with "SFA all order" (blue-dotted line) in the right sub-figure except after electron energy greater then  $12U_p$ . The probability drop rapidly in "SUM" while there exist another plateau in "SFA all order". Just as "SFA2" contributes a plateau at  $3-9U_p$ , the plateau from  $13U_p$  in "SFA all order" can be understood as the contribution from the third and higher order terms corresponding to the KFR theory. After the third-order terms in the KFR theory, it is very difficult to evaluate due to at least 9-fold integration. Our P-space TDSE result consistent with "SFA all order" (right sub-figure) but the R-space TDSE result exhibit a rapidly drop as "SUM" after  $12U_p$  (left sub-figure). We have known that the drop in "SUM" is because only the first two orders of KFR theory

are carried out. How about the drop in the R-space TDSE result? In the R-space TDSE calculation, a finite box in the coordinate space will be set. And the wave function will be filtered out when it reaches the box edge. More higher energy the electron possesses, more larger distant it can travel and hence be filtered out at the box edge. This should be the reason why the photoelectron spectra from R-space TDSE drop rapidly after  $13U_p$ .

We note that SFA only give a qualitative agreement of photoelectron spectra. "SFA1" describe the tunneling process and contribute to the low energy part of photoelectron spectra (below  $2U_p$ ). Coulomb scattering of the ionized electron and ion core contribute to the higher energy plateau. However, the magnitude is smaller than the TDSE result by about 2 orders. The magnitude can be improved by forcing the final state to be orthonormal to the initial state which is called orthonormalized strong-field approximation (OSFA) [52, 68]. In Fig. 2.8, we present the two-dimensional momentum distribution of TDSE and SFA1 (Since Coulomb scattering wouldn't affect low energy distribution in SFA, we only compare SFA1 to TDSE.). Up row are plotted according to Eq. (2.29) which emphasize electron distribution in the direction perpendicular to polarization axis while bottom row plotted according to Eq. (2.30) which emphasize that along the polarization axis.  $p_{\parallel}$  and  $p_{\text{perp}}$  denote the momentum parallel and perpendicular to polarization axis respectively. In Fig. 2.9, we present the energy-angular momentum distribution of TDSE and SFA1 which shows each angular momentum contribution to the photoelectron spectra. From Fig. 2.8 and 2.9, we find SFA give a totally different prediction from TDSE at low energy. Further, the breakdown of SFA is also pointed out in the recent interested mid-infrared regime [22, 23]. It is believed that the low energy electron would be affected by atomic potential significantly. The SFA can be improved by adding the Coulomb correction to Volkov wave function called Coulomb-Volkov wave function [69, 70].

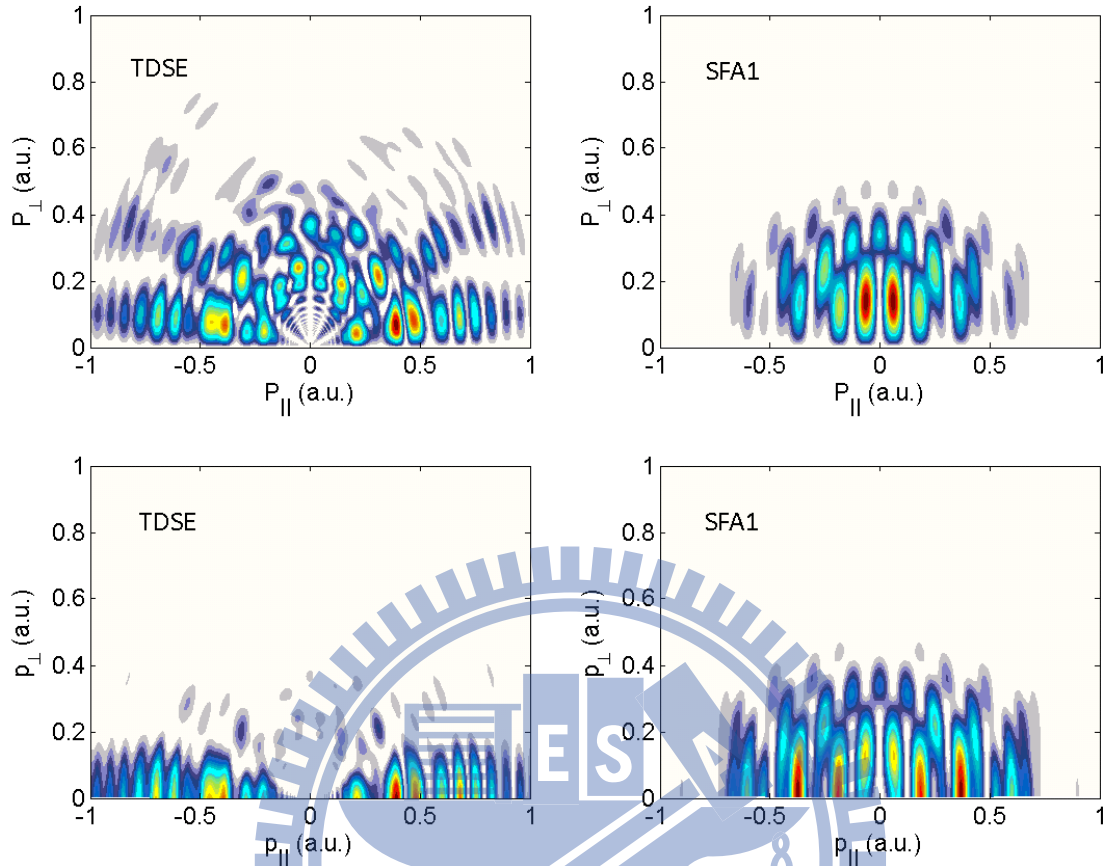


Figure 2.8: Two-dimensional momentum distribution of TDSE and SFA1 of the same system as Fig. 2.7. Up row are plotted according to Eq. (2.29) which emphasize electron distribution in the direction perpendicular to polarization axis while bottom row plotted according to Eq. (2.30) which emphasize that along the polarization axis.  $p_{\parallel}$  and  $p_{\perp}$  denote the momentum parallel and perpendicular to polarization axis, respectively.

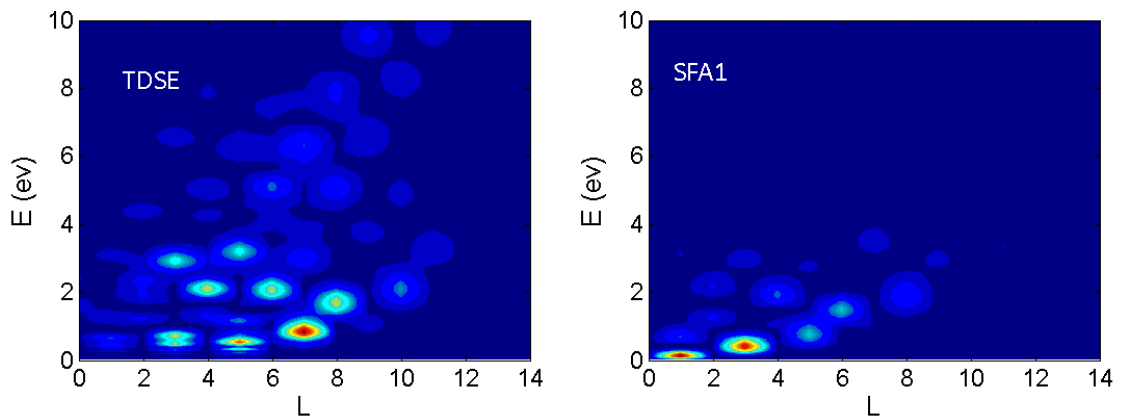


Figure 2.9: Energy-angular momentum distribution of TDSE and SFA1 of the same system as Fig. 2.7 which shows each angular momentum contribution to the photoelectron spectra.

## Chapter 3

# Strong-field Ionization of a Lithium Atom

In the section 3.1, we compare our calculation results to experimental results for calibration. To compare to experimental results, we need to average the signals of ionized electron from different atoms in the different region of the laser-focal volume (hence feel different laser intensity). Since the volume-averaged results contain so many signals, it is not convenient to analyze the underlying mechanism inside. In the section 3.2, we present the results at a single peak intensity (or without laser-focal volume average). In the section 3.3, we will discuss the multiphoton ionization (MPI) at relatively small intensities, including nonresonant multiphoton ionization (NRMPI), dynamical resonant multiphoton ionization (DRMPI), and ponderomotive shift. In the section 3.4, we will discuss the generation of Rydberg states in the lithium atom. In the section 3.5, we will discuss the fan structure in the direction perpendicular to polarization axis.

### 3.1 Compare with experimental results

Before comparing to experimental results [51], we need to discuss laser-focal volume average first. The focus of a actual laser beam is not a spot but has a volume. When we talk about the laser peak intensity  $I_0$  of a laser beam, we always mean the value at the cental of the laser-focal volume. And, laser intensity decays gradually outward. The spatial distribution of the laser intensity can be formulated as Lorentzian in the propagation direction ( $z$ ) and Gaussian in the transverse direction ( $\rho$ ) [71, 72]:

$$I(r, z) = \frac{I_0 w_0^2}{w^2(z)} e^{-2r^2/w^2(z)} \quad (3.1)$$

$$w(z) = w_0 \sqrt{1 + \left(\frac{z}{z_R}\right)^2} \quad (3.2)$$

where  $w_0$  is the radius of the focal spot and  $z_R$  is the Rayleigh range of the focus. In Fig. 3.1, we show the Iso-intensity surface plot of a laser-focal volume. We assume the gas

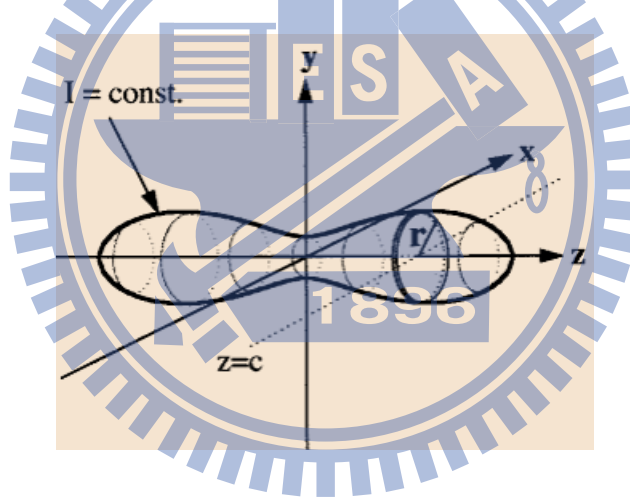


Figure 3.1: Iso-intensity surface plot of a laser-focal volume,  $z$  is the propagation direction. This figure is from Ref. [72].

volume is filled over the laser-focal volume, then the ejected electron signals are the sum of electrons ionized from atom at different intensity region of the laser-focal volume. For a peak intensity  $I_0$ , the ejected electron signals with momentum  $\mathbf{p}$  is given by [71]:

$$S(\mathbf{P}, I_0) = D \int_0^{I_0} P_I(\mathbf{P}) \left( -\frac{\partial V}{\partial I} \right) dI \quad (3.3)$$

where  $D$  is the density of the target atoms,  $P_I(\mathbf{P})$  is the ionization probability for a particular intensity  $I$ , and  $\left( -\frac{\partial V}{\partial I} \right) dI$  is the volume element between  $I$  and  $I+dI$  iso-intensity surface. The volume element for the laser beam of Eq. (3.1) is given as

$$-\frac{\partial V}{\partial I} dI = \frac{\pi w_0^3 z_0}{3} \frac{1}{I} \left( \frac{I_0}{I} + 2 \right) \sqrt{\frac{I_0}{I} - 1} dI \quad (3.4)$$

The trapezoidal rule are used for the integration over intensity.

Now, we return to compare with experiment results. The experiment was carried out with a linear polarized laser pulse of wavelength 785nm, FWHM 30fs, and peak intensity  $I_0$  ranging from  $4 \times 10^{11} W/cm^2$  ( $\gamma = 11.6$ ) to  $7 \times 10^{13} W/cm^2$  ( $\gamma = 0.8$ ) which is from multiphoton ionization regime ( $\gamma > 1$ ) to tunneling ionization regime ( $\gamma < 1$ ).

We adopt the following model potential for a lithium atom [73].

$$V(r) = -\frac{1}{r} - \frac{a_1 e^{-a_2 r} + a_3 r e^{-a_4 r}}{r} \quad (3.5)$$

where  $a_1 = 2$ ,  $a_2 = 3.395$ ,  $a_3 = 3.212$ , and  $a_4 = 3.207$ . In our calculation, we use 1024 grid points,  $l_{max} = 14$ ,  $\Delta t = 0.2$  (a.u.) and the laser-focal volume average is carried out as: For peak intensity  $I_0 = 4 \times 10^{11} W/cm^2$  and  $I_0 = 8 \times 10^{11} W/cm^2$ , we integrate from  $5\% \times I_0$  to  $I_0$  and  $\Delta I = 0.2 \times 10^{11} W/cm^2$ . For peak intensity  $I_0 = 7 \times 10^{13} W/cm^2$ , we integrate from  $2.8\% \times I_0$  to  $I_0$  and  $\Delta I = 0.1 \times 10^{13} W/cm^2$ . All others are integrated from  $5\% \times I_0$  to  $I_0$  and  $\Delta I = 0.1 \times 10^{12} W/cm^2$ .

In Fig. 3.2 and 3.3, we show the two-dimensional momentum distribution of our results (left column) and experiment results (right column) for seven different peak intensity ranging from multiphoton ionization regime ( $\gamma > 1$ ) to tunneling ionization regime ( $\gamma < 1$ ). In Fig. 3.4 and 3.5, we show the photoelectron spectra with laser parameters corresponding to Fig. 3.2 and 3.3. Our results agree well with experiment results.

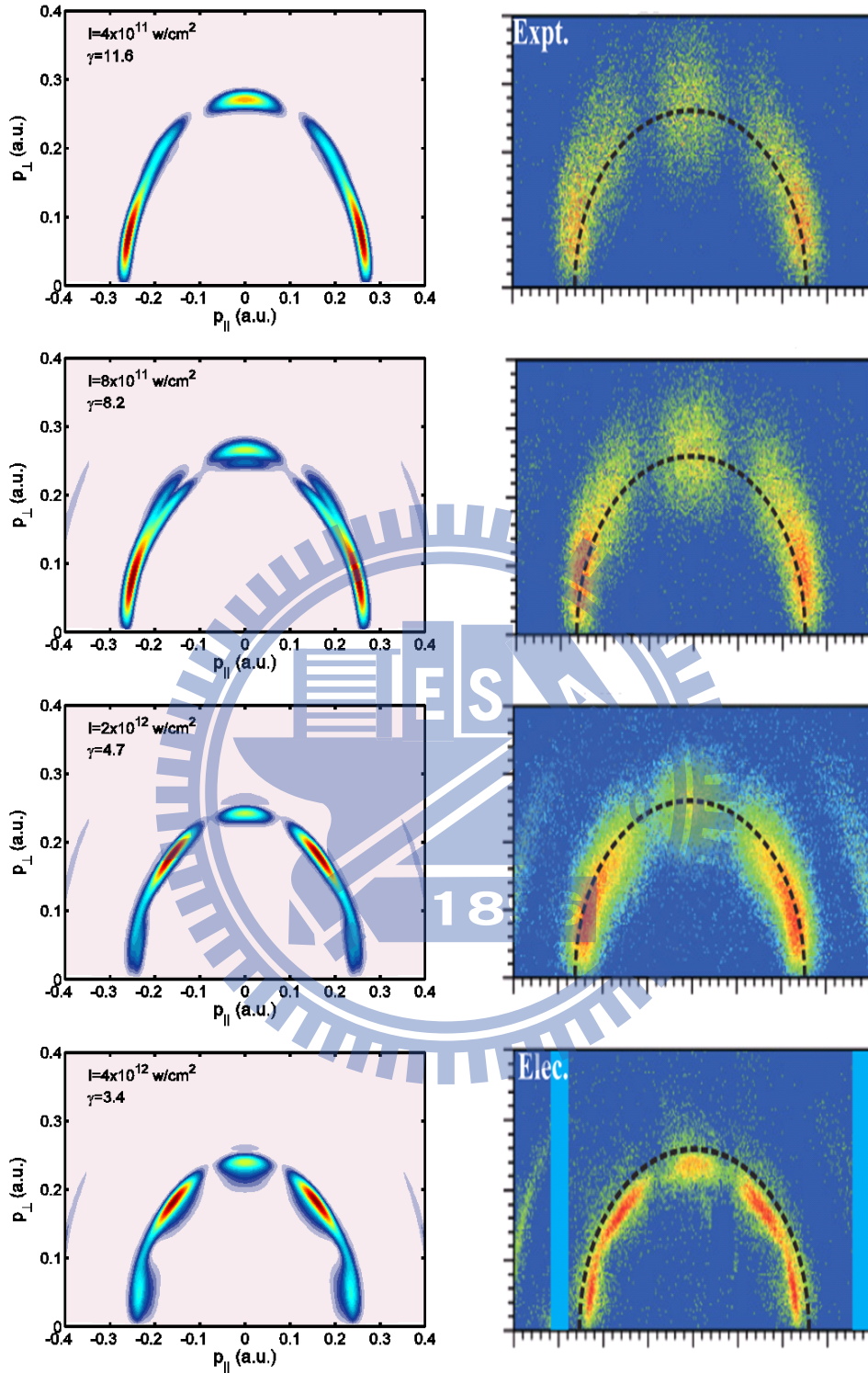


Figure 3.2: Two-dimensional momentum distribution of a lithium atom with a linear polarized laser pulse with FWHM 30fs, wavelength 785nm, and peak intensity  $4 \times 10^{11} W/cm^2$ ,  $8 \times 10^{11} W/cm^2$ ,  $2 \times 10^{12} W/cm^2$ , and  $4 \times 10^{12} W/cm^2$  (from up to bottom). Left column is our results and right column is experimental results from Ref. [51].  $p_{\parallel}$  and  $p_{\perp}$  denote the momentum parallel and perpendicular to polarization axis, respectively.



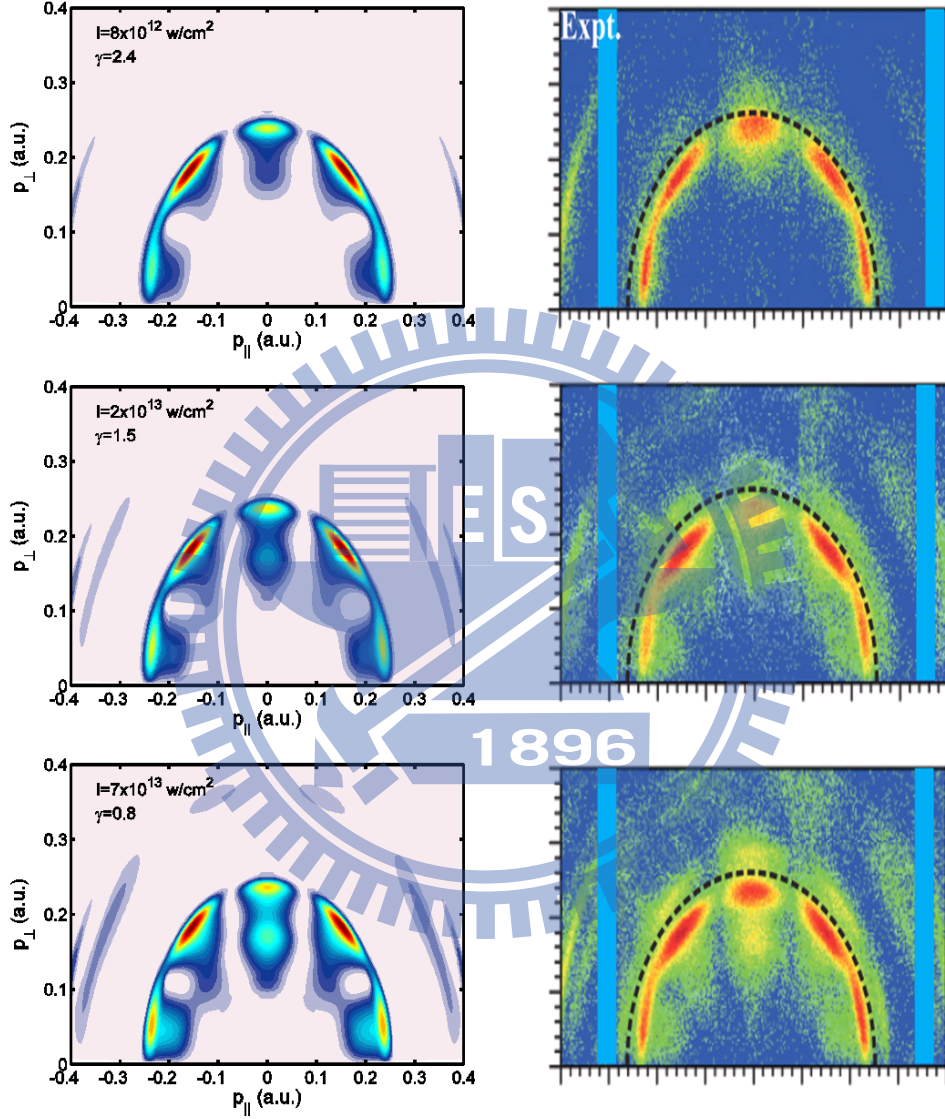


Figure 3.3: The same as Fig. 3.2 but now laser peak intensity  $8 \times 10^{12} \text{ W/cm}^2$ ,  $2 \times 10^{13} \text{ W/cm}^2$ , and  $7 \times 10^{13} \text{ W/cm}^2$  (from up to bottom). Left column is our results and right column is experimental results from Ref. [51].  $p_{\parallel}$  and  $p_{\perp}$  denote the momentum parallel and perpendicular to polarization axis, respectively.

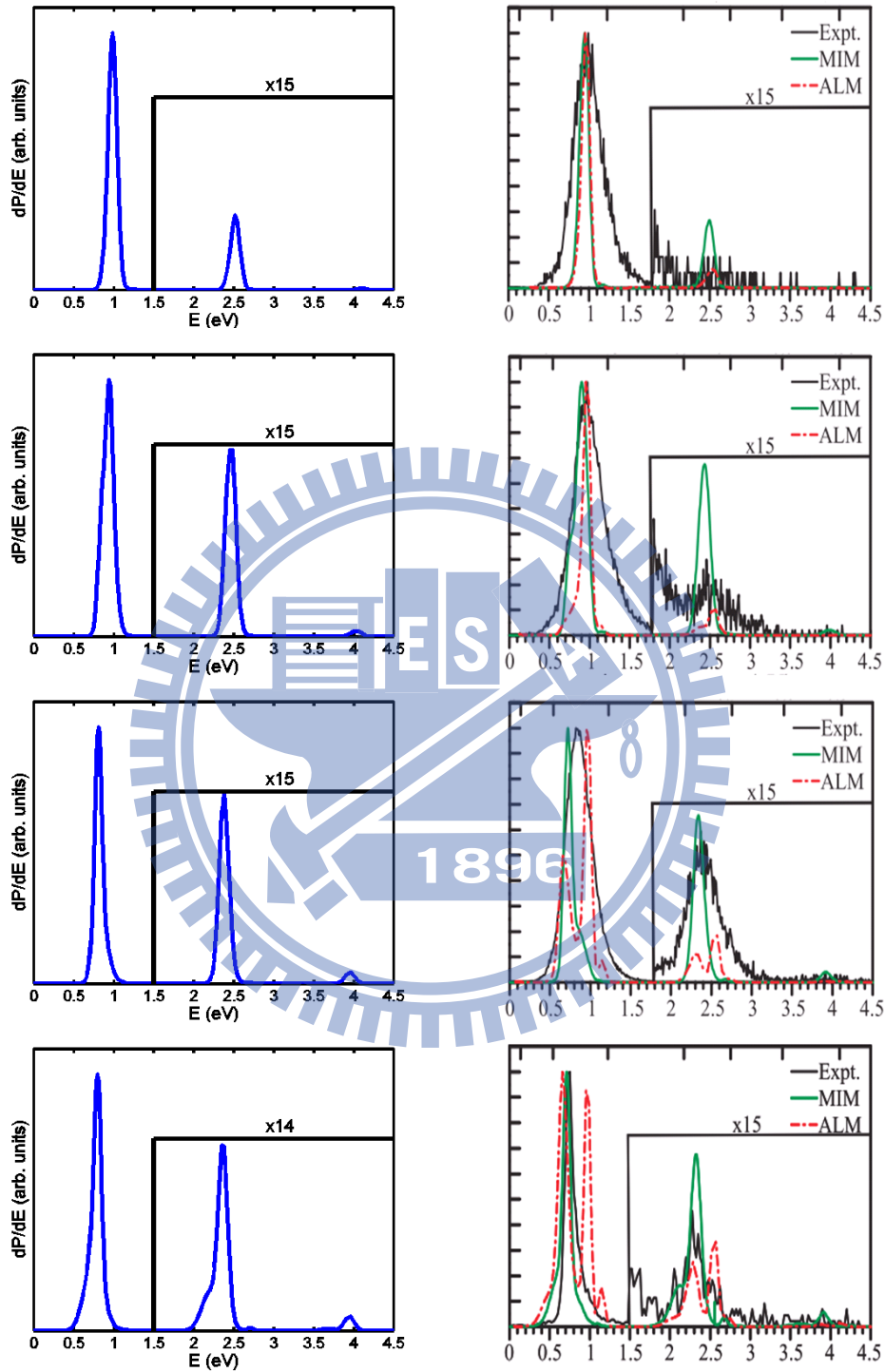


Figure 3.4: Photoelectron spectra of a lithium atom with a linear polarized laser pulse with FWHM 30fs, wavelength 785nm, and peak intensity  $4 \times 10^{11} W/cm^2$ ,  $8 \times 10^{11} W/cm^2$ ,  $2 \times 10^{12} W/cm^2$ , and  $4 \times 10^{12} W/cm^2$  (from up to bottom). Left column is our results and right column is experimental results from Ref. [51].

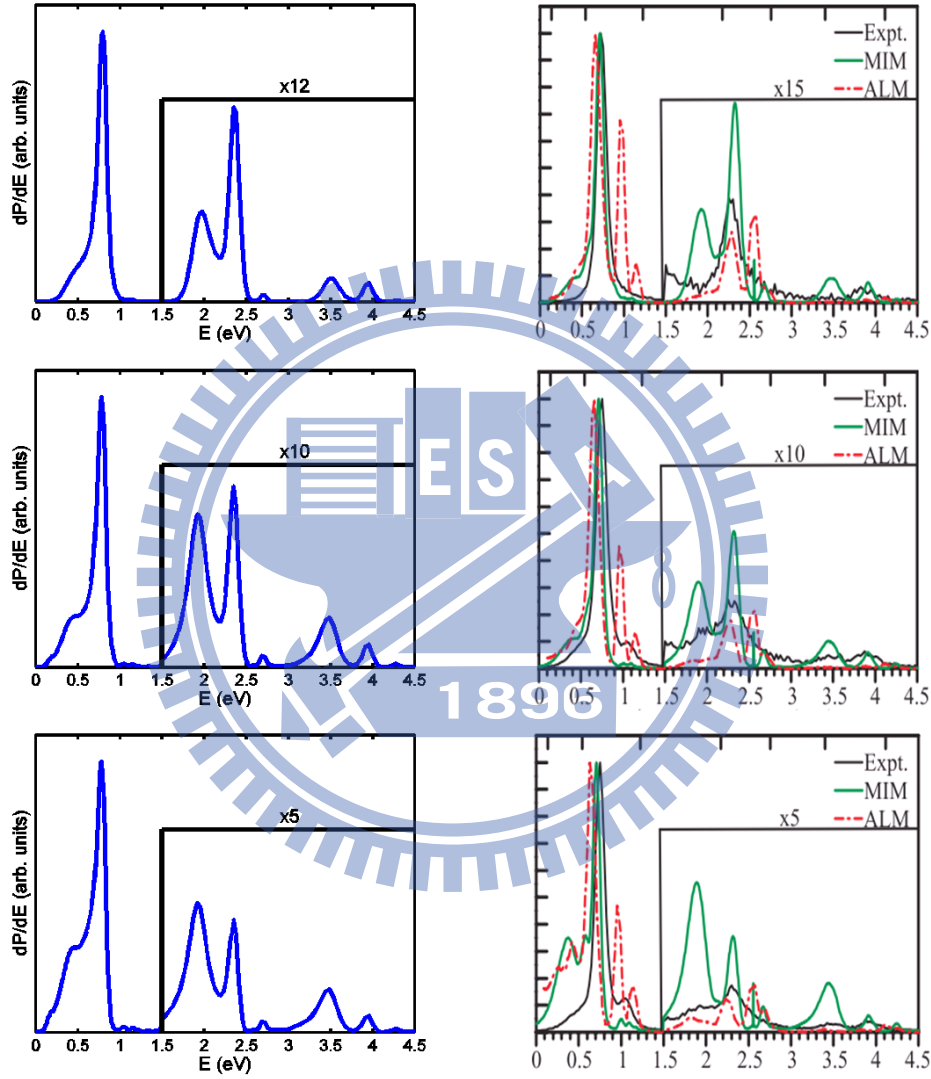


Figure 3.5: The same as Fig. 3.4 but now laser peak intensity  $8 \times 10^{12} W/cm^2$ ,  $2 \times 10^{13} W/cm^2$ , and  $7 \times 10^{13} W/cm^2$  (from up to bottom). Left column is our results and right column is experimental results from Ref. [51].

## 3.2 Features of strong-field ionization of a lithium atom

Since the volume-averaged results contain so many signals from different atoms which feel different laser intensity, it is not convenient to analyze the underlying mechanism inside. In this section and after, we will discuss the results at a single peak intensity with the same laser parameters as the experiment where wavelength 785nm, FWHM 30fs, and intensity ranging from  $4 \times 10^{11} \text{W/cm}^2$  ( $\gamma = 11.6$ ) to  $7 \times 10^{13} \text{W/cm}^2$  ( $\gamma = 0.8$ ). In addition, we also study the short pulse cases with FWHM 10fs and 6fs.

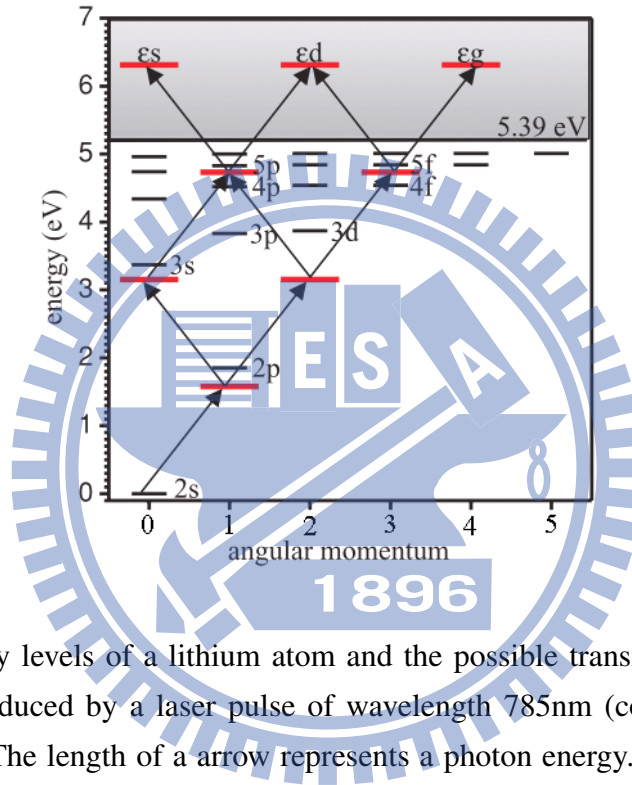


Figure 3.6: Energy levels of a lithium atom and the possible transition pathways from ground state 2s induced by a laser pulse of wavelength 785nm (correspond to photon energy 1.57 eV). The length of a arrow represents a photon energy. This figure is from Ref. [51].

In Fig. 3.6, we show the energy level of a lithium atom and the possible transition pathways from ground state 2s induced by a laser pulse of wavelength 785nm (corresponds to photon energy 1.57 eV). The length of a arrow means a photon energy. According to selection rule, only those transitions satisfying  $\Delta l = \pm 1$  are allowed for absorbing a photon. In this figure, we find that the electron can be ionized by absorbing 4 photons. The first peak of ionized electron should be at  $\sim 0.9$  eV in energy (or 0.26 a.u. in momentum  $|p|$ ) and composed of  $l = 0, 2,$  and 4 partial waves. The most probably involved intermediate bound states are 2p, 3s, 4p, 4f, 5p, and 5f.

In Fig. 3.7, we present the two-dimensional momentum distribution without volume average for 30fs pulse. Let's make some observation first. At smaller intensities, (a) and (b), we observe a 4-photon ionization ring. The number of nodes in the ring (except the two near x-axis) result from the zeros of Legendre polynomial  $P_l(\cos\theta)$  and thus indicate

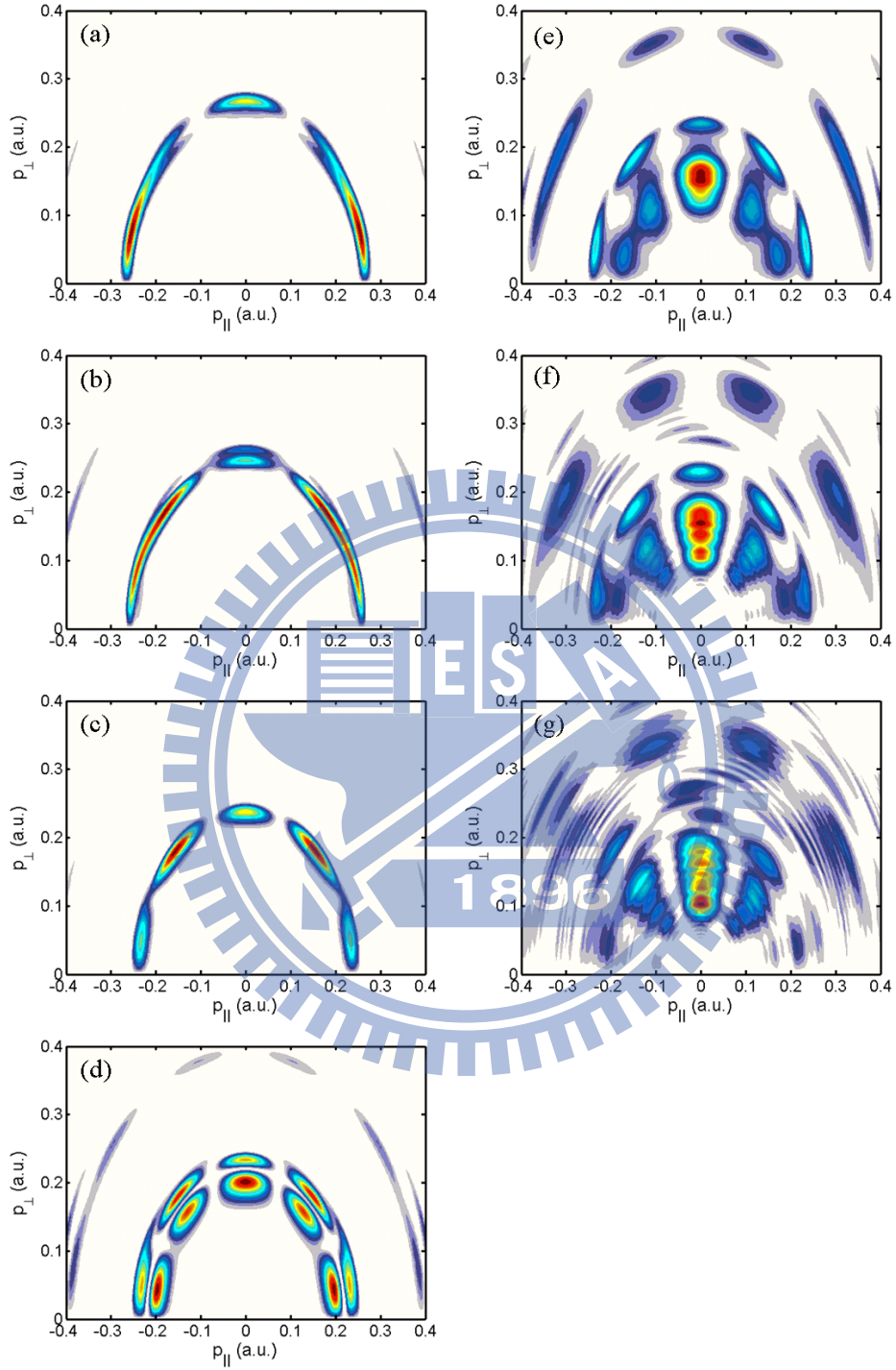


Figure 3.7: Two-dimensional momentum distribution of a lithium atom with a linear polarized laser pulse FWHM 30fs, wavelength 785nm, and peak intensity:(a) $4 \times 10^{11}W/cm^2$ , (b) $8 \times 10^{11}W/cm^2$ , (c) $2 \times 10^{12}W/cm^2$ , (d) $4 \times 10^{12}W/cm^2$ , (e) $8 \times 10^{12}W/cm^2$ , (f) $2 \times 10^{13}W/cm^2$ , and (g) $7 \times 10^{13}W/cm^2$ .  $p_{\parallel}$  and  $p_{\perp}$  denote the momentum parallel and perpendicular to polarization axis, respectively.

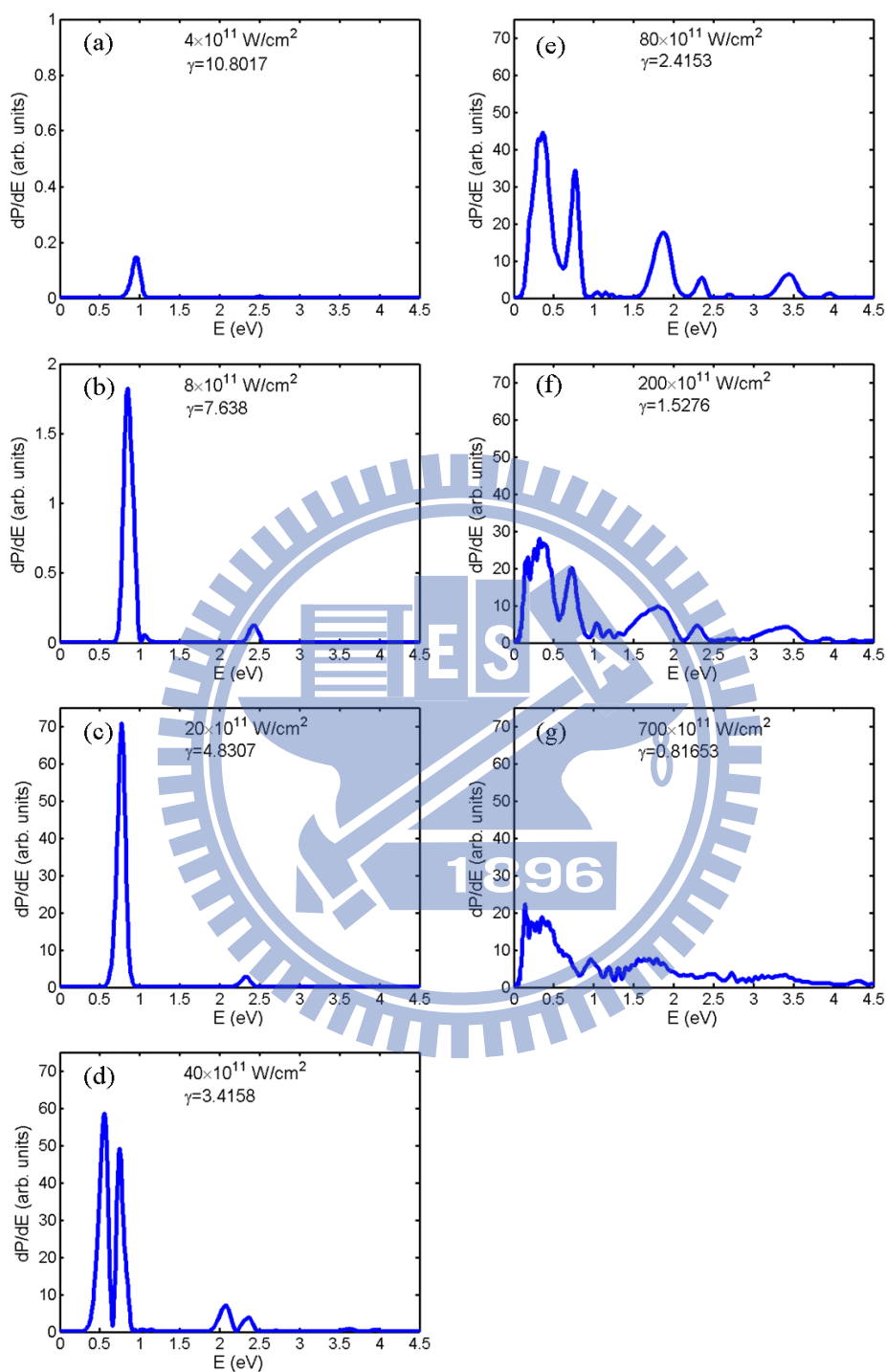


Figure 3.8: Photoelectron spectra of a lithium atom with a linear polarized laser pulse FWHM 30fs, wavelength 785nm, and peak intensity:(a)  $4 \times 10^{11} \text{ W/cm}^2$ , (b)  $8 \times 10^{11} \text{ W/cm}^2$ , (c)  $2 \times 10^{12} \text{ W/cm}^2$ , (d)  $4 \times 10^{12} \text{ W/cm}^2$ , (e)  $8 \times 10^{12} \text{ W/cm}^2$ , (f)  $2 \times 10^{13} \text{ W/cm}^2$ , and (g)  $7 \times 10^{13} \text{ W/cm}^2$ .

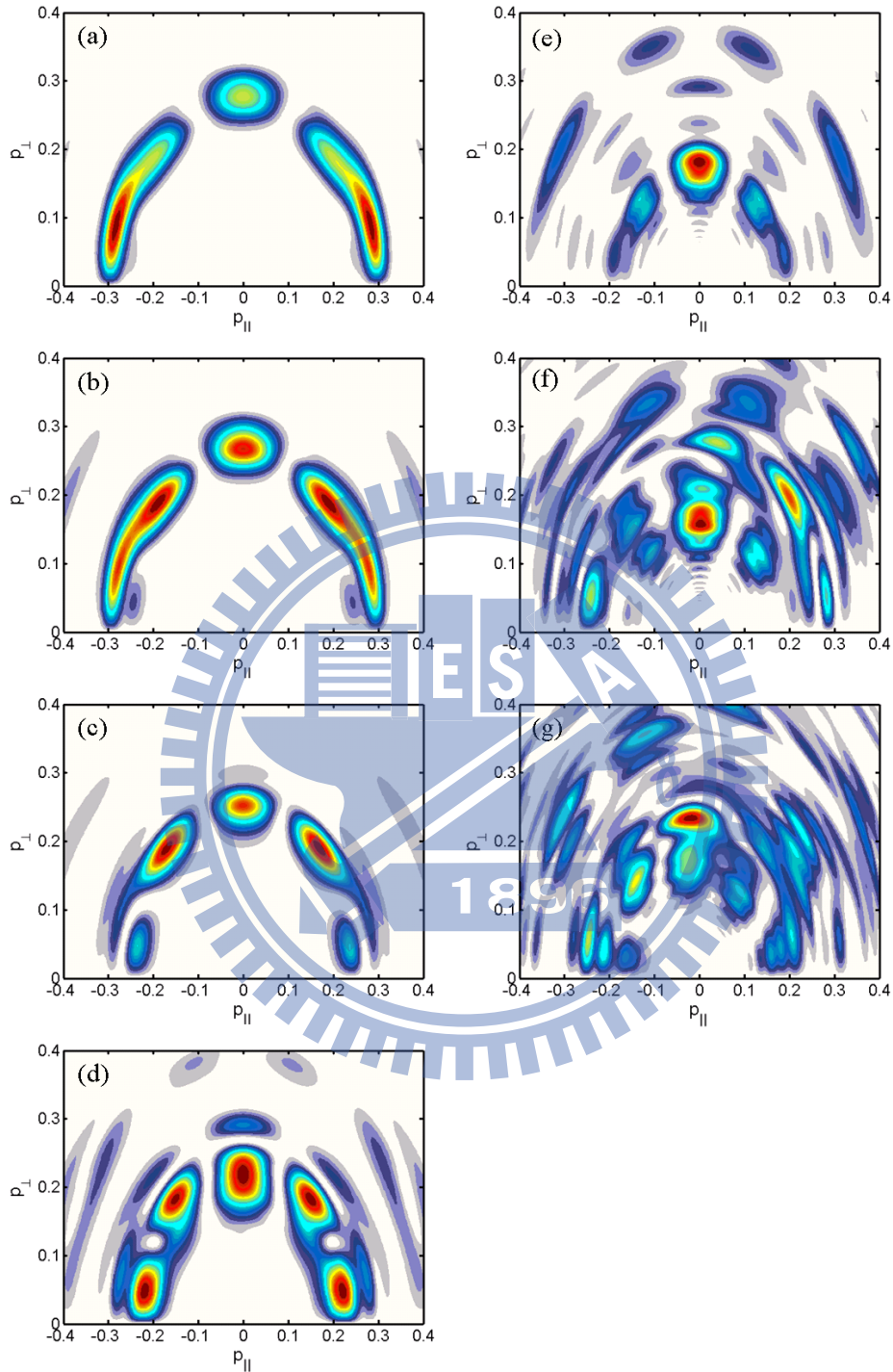


Figure 3.9: Two-dimensional momentum distribution of a lithium atom with a linear polarized laser pulse FWHM 10fs, wavelength 785nm, and peak intensity:(a) $4 \times 10^{11}W/cm^2$ , (b) $8 \times 10^{11}W/cm^2$ , (c) $2 \times 10^{12}W/cm^2$ , (d) $4 \times 10^{12}W/cm^2$ , (e) $8 \times 10^{12}W/cm^2$ , (f) $2 \times 10^{13}W/cm^2$ , and (g) $7 \times 10^{13}W/cm^2$ .  $p_{||}$  and  $p_{\perp}$  denote the momentum parallel and perpendicular to polarization axis, respectively.

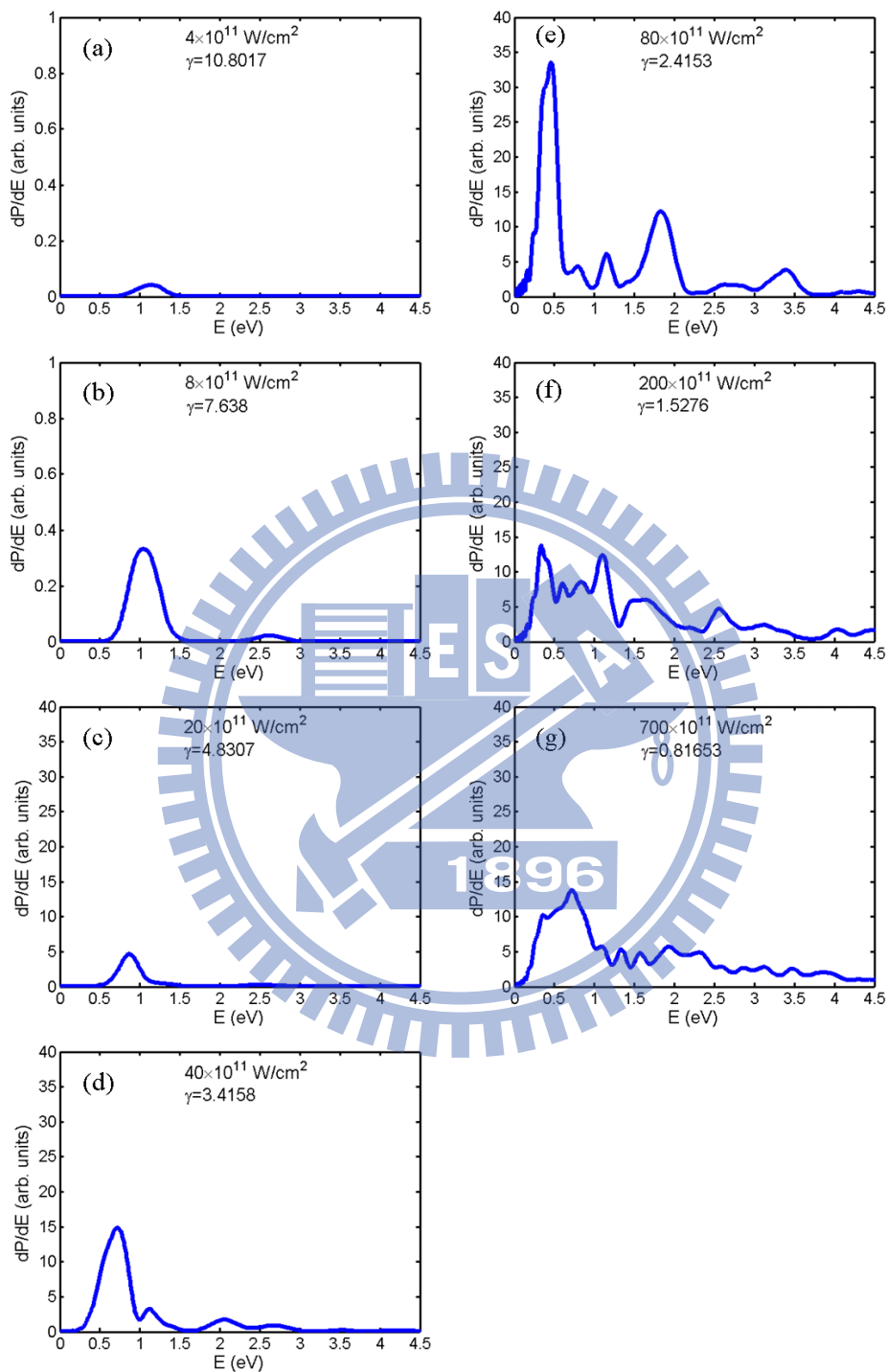


Figure 3.10: Photoelectron spectra of a lithium atom with a linear polarized laser pulse FWHM 10fs, wavelength 785nm, and peak intensity:(a)  $4 \times 10^{11} W/cm^2$ , (b)  $8 \times 10^{11} W/cm^2$ , (c)  $2 \times 10^{12} W/cm^2$ , (d)  $4 \times 10^{12} W/cm^2$ , (e)  $8 \times 10^{12} W/cm^2$ , (f)  $2 \times 10^{13} W/cm^2$ , and (g)  $7 \times 10^{13} W/cm^2$ .



which partial wave is dominant. In (a) and (b), the  $l = 2$  partial wave is dominant, since there are two nodes in the ring. For (c), still a 4-photon ionization ring but  $l = 4$  is dominant now. In addition, we find that the radius of the ring become smaller than (a) and (b). For (d), another ring appears inside the original one. From (e) to (g), the inner ring extend radially inward and resulting a fanlike structure. And, we find the electron is distributed to the direction perpendicular to the polarization axis gradually. This is strange since the motion of the electron will be driven by the laser field and there should be a more probability along the polarization axis.

In Fig. 3.8, we present the corresponding photoelectron spectra of Fig. 3.7. The first peak corresponds to the evident ring in Fig. 3.7. The following peak in (a), (b), and (c) is the associated 5-photon peak by absorbing one more photon from the former one hence differ by about a photon energy (1.57 eV). After (d), more peaks appear, where are they coming from?

In Fig. 3.9, we present the two-dimensional momentum distribution without volume average for 10fs pulse. At first glance, the features are similar to 30fs cases for (a) to (e) with a broader band, which is due to the uncertainty principle  $\Delta E \Delta t > 1$ . The shorter (longer) the time duration of a pulse, the broader (narrower) the energy spectra. Inspection further, we find that the position of the double peaks in (d) is different from that in 30fs case. For (f) and (g), we find that two-dimensional momentum distribution is no loner symmetric. This can be understood as the contribution from tunneling ionization which is believed to be dominant at higher intensity (or smaller  $\gamma$ ). Tunneling ionization is directional with the oscillation of a laser field and thus resulting asymmetric in the two-dimensional momentum distribution, especially for shorter pulse.

In Fig. 3.10, we present the corresponding photoelectron spectra of Fig. 3.9. The same as Fig. 3.8, the first peak corresponds to the evident ring in Fig. 3.9. and the two peaks in (a), (b), and (c) are associated 4-photon and 5-photon peaks. After (d), more peaks appear, but somewhat different from that in Fig. 3.8. Where are they coming from?

In Fig. 3.11, we present the ionization probability vs Keldysh parameter ( $\gamma$ ) for 6 fs, 10fs, and 30fs pulse. The vertical line at  $\gamma = 3.7$  is the critical value of the classical OBI. It seems there is no dramatic behavior happening near this point. At  $\gamma = 2.5$  and lower, the behavior of the ionization probability curves have significant changes for all three cases: For 30fs pulse, with the decrease of  $\gamma$ , we observe the ionization trapping and then suppression. For 10fs pulse, similar to 30fs initially, but the ionization probability recover and exhibits an oscillation in the end. For 6fs pulse, the ionization rate trends to smooth and also exhibit an oscillation in the end. Besides we also observe a ionization trapping around  $\gamma = 4.5$  for 30fs pulse.

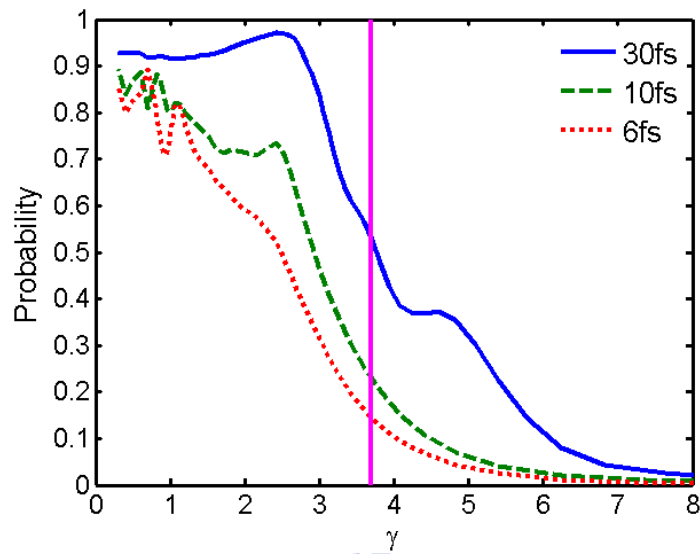
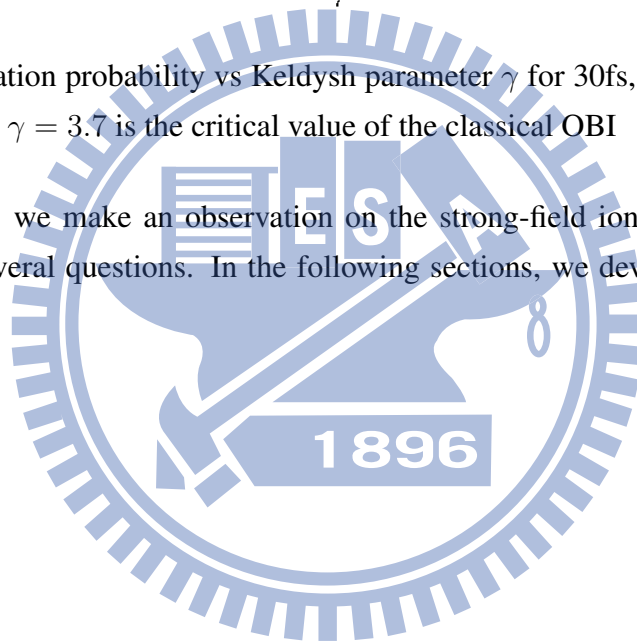


Figure 3.11: Ionization probability vs Keldysh parameter  $\gamma$  for 30fs, 10fs, and 6fs pulse. The vertical line at  $\gamma = 3.7$  is the critical value of the classical OBI

In this section, we make an observation on the strong-field ionization of a lithium atom and leave several questions. In the following sections, we devote to answer these questions.



### 3.3 Multiphoton ionization (MPI)

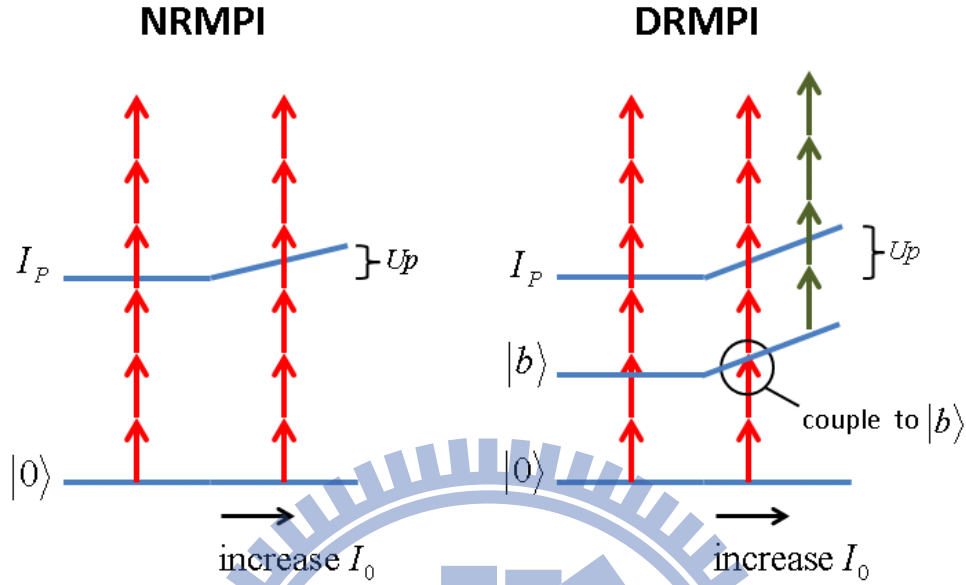


Figure 3.12: Schematic plot of the NRMPI and DRMPI processes.  $|0\rangle$  is the ground state,  $|b\rangle$  is any intermediate bound state,  $I_P$  is ionization potential,  $I_0$  is laser intensity, and  $U_p$  is ponderomotive shift.

In this section, we devote to trace the peaks in the photoelectron spectra. We begin by introducing two multiphoton ionization processes: nonresonant multiphoton ionization (NRMPI) and dynamical resonant multiphoton ionization (DRMPI). In Fig. 3.12, we show the schematic plot of these two processes.

Nonresonant multiphoton ionization (NRMPI) : NRMPI means the electron in the ground state absorbs enough photons to exceed the ionization potential and doesn't hit any intermediate bound state. Directly follow the idea of photoelectric effect, then the photoelectron energy  $\varepsilon_k$  should be:

$$\varepsilon_k = n\hbar\omega - I_P \quad (3.6)$$

where  $I_P$  is ionization potential,  $n$  is a number greater or equal to the minimum number of photons needed to exceed the ionization potential, and  $\hbar\omega$  is a photon energy. However, Eq. (3.6) work only at smaller laser intensity. This is because ionization threshold will increase by an amount of  $U_p$  effectively in the laser field [74, 75].  $U_p = E_0^2/4\omega^2$  is ponderomotive energy which is the average kinetic energy of an electron in the laser field.  $U_p$  increase with laser intensity and can be neglected at smaller intensity. This effectively upshift of ionization threshold can be understood as: After overcome the ionization potential, the electron can still not be regarded as ionized until it possesses the average kinetic

energy  $U_p$  in the field. And, Eq. (3.6) should be modified as:

$$\varepsilon_k = n\hbar\omega - I_P - U_p \quad (3.7)$$

Dynamical resonance multiphoton ionization (DRMPI) [10] : In the schematic plot of the NRMPI, except the ground state, other bound states are neglected. In the right sub-figure of Fig. 3.12, we add a bound state and there is nothing change if we carefully control the laser frequency to avoid hitting the bound state. However, as the ionization threshold would be changed effectively in a laser field, the atomic energy levels would also be changed in the laser field which is known as ac-Stark shift. At lower intensity,  $|b\rangle$  is not coupled. With the increase of laser intensity, energy level  $|b\rangle$  would shift during the pulse time and is possible to be hit during the laser pulse time. Strong coupling or resonance between ground state and bound state may cause a considerable amount of occupation to the bound state, and further ionized from that bound state. Such process is called DRMPI. For low lying states, the energy shift depends on the dynamics polarizability of the states [76]. For higher atomic levels, the energy shift is roughly equal to ponderomotive shift ( $U_p$ ). Therefore, the photoelectron peak from intermediate bound states through DRMPI behaves almost steady with increasing laser intensity [10] while that from NRMPI will "run" with increasing laser intensity. This is a useful clue to identify where a multiphoton peak comes from.

In the following, we introduce another useful tool to identify the multiphoton peaks. That is separation of the photoelectron spectra into odd and even angular momentum parts. Since one photon absorption is only allowed between states satisfying the selection rule  $\Delta l = \pm 1$ . Given a initial state with even angular momentum, the next states must be composed of odd angular momentum by absorbing one photon. The further next states must be even again after absorbing one more photon and so on. Therefore, multiphoton peaks must be composed of either even angular momentum or odd angular momentum and adjacent peaks even-odd change alternatively (Refer to Fig. 3.6).

In Fig. 3.13, we present two cases for example. Both are lithium atom under 785 wavelength, 10fs FWHM pulse but different intensity. Up row are original results, contain all angular momentum. In the bottom row, we separate the photoelectron spectra into odd and even angular momentum parts. In the left sub-figure, it is not difficult to distinguish the two peaks even in the original plot (up left). The peaks at  $\sim 0.9$  eV is the 4-photon peak and the one at  $\sim 2.5$  eV is the 5-photon peak. They differ by about a photon energy (1.57 eV). Check the angular momentum component (left bottom), the 4-photon peak is contributed from even angular momentum part while 5-photon peak from odd angular momentum part. At larger intensity, situation becomes more complicated (right up). However, by separating the photoelectron spectra into odd and even angular momentum

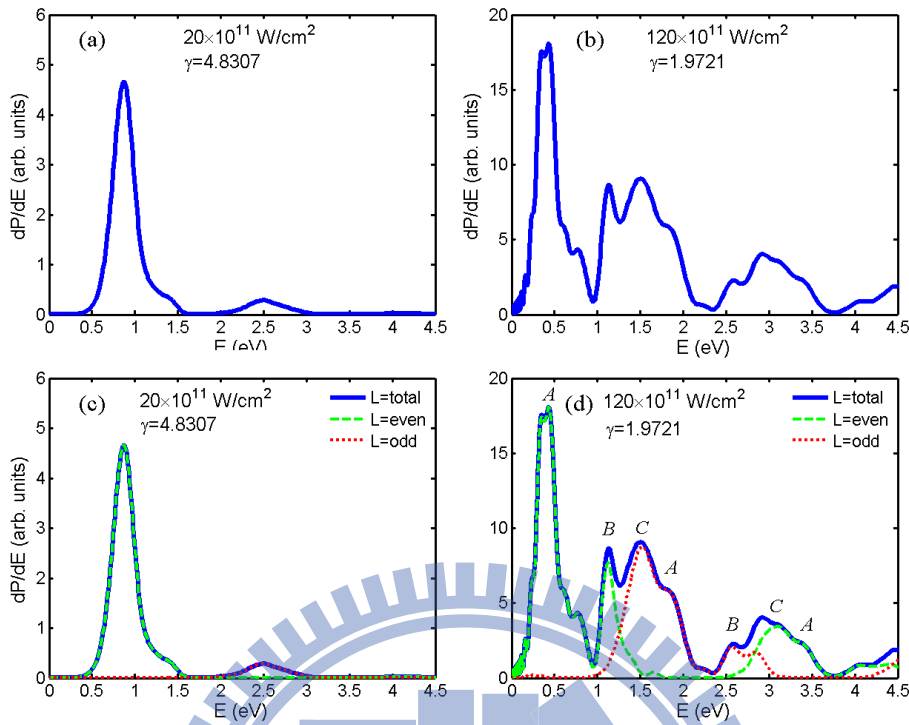


Figure 3.13: Photoelectron spectra of a lithium atom with a linear polarized laser pulse FWHM 10fs, wavelength 785nm, and peak intensity:  $20 \times 10^{11} W/cm^2$  (left column) and  $120 \times 10^{11} W/cm^2$  (right column). The up row contain all angular momentum components while we separate the angular momentum into even and odd parts in the bottom row.

parts (right bottom), we can distinguish three different ATI groups, A, B, and C easily by two principles : (a) choose a peak, the next associated peak (absorbing one more photon) must differ in color. (b) Their energy differ by a photon energy (1.57 eV). Further, we can identify the first B peak is a 4-photon peak which is hard to tell in the original plot (right up). Therefore, we can know that the green-dash line ranging from 0 eV to 1.5 eV is a 4-photon group and the red-dotted line ranging from 1 eV to 3 eV is a 5-photon group.

### 3.3.1 Examination of the spectra for 30fs pulse

Now, we return to examine the multiphoton peaks for 30fs pulse. In Fig. 3.8 (a), (b), and (c), we find the first peak move to lower energy with increasing intensity, so this is a NRMPI peak from ground state 2s by absorbing 4 photons. The second peak is its associated 5-photon ATI peak. In (d), another peak appears and forms a doubles peaks structure. One at  $\sim 0.5$  eV and the other at 0.7-0.8 eV. To trace it origin, it is helpful to separate the photoelectron spectra into odd and even angular momentum parts as well as examine the population history of those relevant bound states. In Fig. 3.14, we show the population history of the some relevant bound states (left), and the photoelectron spectra

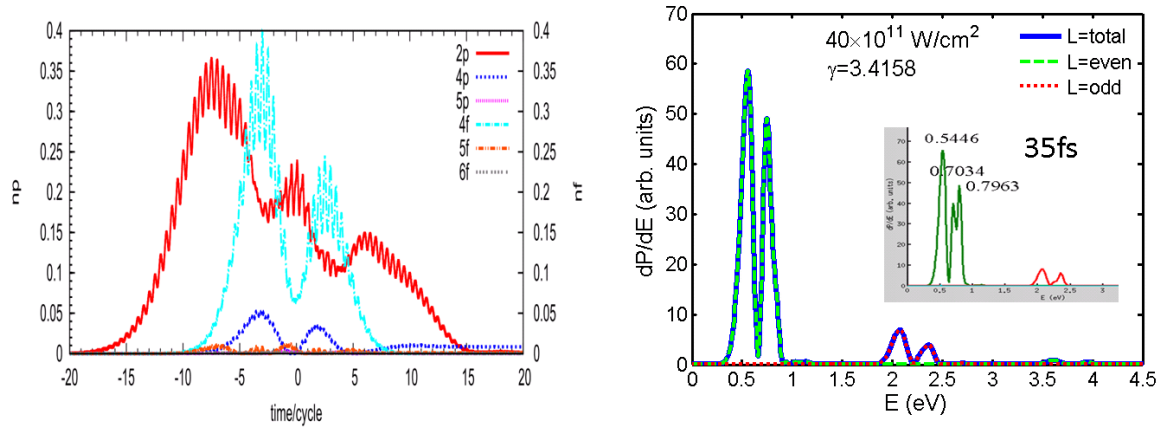


Figure 3.14: Population history of some relevant bound states (left) and photoelectron spectra (right) of a lithium atom with a linear polarized laser pulse FWHM 30fs, wavelength 785nm, and peak intensity  $40 \times 10^{11} W/cm^2$ . Inset in the right sub-figure is the photoelectron spectra for 35fs pulse.

in odd and even angular momentum parts (right). From the population history, we find the 2p, 4p, and 4f are strongly coupled. So, we expect there should be two peaks at 0.7-0.8 eV. One is from ground state 2s by absorbing 4 photons through NRMPI (Eq. 3.7), and the other is from 4p and 4f by absorbing 1 photon through DRMPI. Since 4p and 4f are nearly degenerate, and can be thought of contributing to the same peak. These two pathways all give even angular momentum to their first ionized peaks. However, in the photoelectron spectra (right), we only find a peak at 0.7-0.8 eV. To check further, we use a longer pulse (35fs), hence has a higher resolution in energy spectrum. In the inset, we actually find two peaks at 0.7-0.8 eV, thus confirm our scenario. For the peak at  $\sim 0.5$  eV, we think it mainly from the 2p by absorbing 3 photons. Let's go back to check the energy levels in Fig. 3.6 first.  $E_{2p} - E_{2s} > a$  photon energy, therefore the 2p state should have ac-Stark downshift as so to couple to 2s state and largely occupied at the -10 cycles of the pulse time [Fig. 3.14 (left)]. The ac-Stark downshift of 2p state should be at least 0.25 eV. And, according to Eq. (3.8), the peak from 2p through DNMPI should be at  $\sim 0.5$  eV, which agree with what we have observed. The double peaks at 2-2.5 eV is the associated 5-photon ATI peaks of the former 4-photon peaks.

### 3.3.2 Examination of the spectra for 10fs pulse

For the 10fs pulse, just the same as 30fs case, the first peak at (a), (b), and (c) in Fig. 3.10 is from 2s by absorbing 4 photons through NRMPI. For (d), by checking the population history in Fig. 3.15, the more active states are 2p, 4p, and 5f. [see also the angular momentum analysis. Fig. 3.16 (b)] Similar to 30fs case, the peak at  $\sim 0.7$  eV with broader

bandwidth contains the contribution from 2s by absorbing 4 photons through NRMPI, from 2p by absorbing 3 photons through DRMPI, and from 4p and 4f by absorbing 1 photon through DRMPI. In addition, there is still a small peak at  $\sim 1.2$  eV, this is from the 5f by absorbing 1 photon through DRMPI.

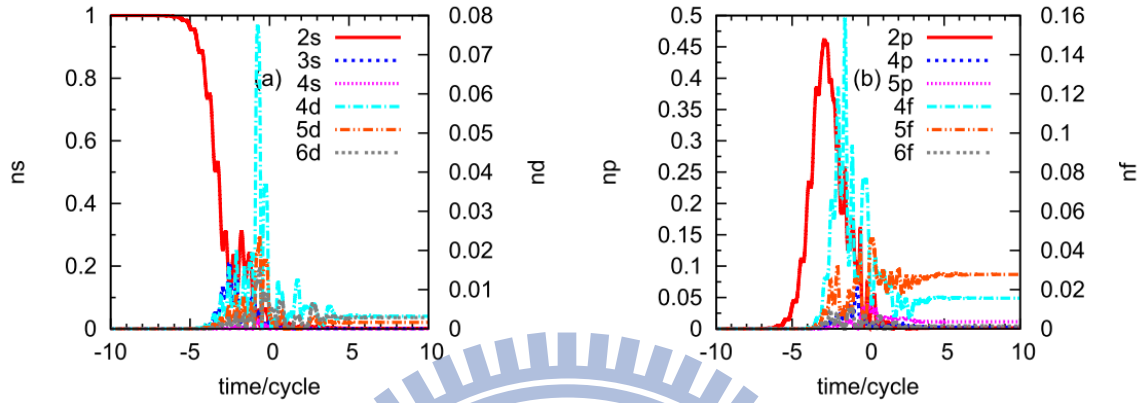


Figure 3.15: Population history of some relevant bound states of a lithium atom with a linear polarized laser pulse FWHM 10fs, wavelength 785nm, and peak intensity  $40 \times 10^{11} W/cm^2$ .

Further, we find a transition from direct 4-photon ionization to direct 5-photon ionization from bound states for 10fs pulse. This is not a unique process for 10fs pulse, but it is more easy to observe in the 10fs case. In Fig. 3.16, we show the photoelectron spectra for 10fs pulse from intensity  $20 \times 10^{11} W/cm^2$  and increase gradually to  $120 \times 10^{11} W/cm^2$ . In Fig. 3.16 (a), with intensity  $20 \times 10^{11} W/cm^2$ , we can observe a 4-photon peak A at  $\sim 0.9$  eV. In (b), with intensity  $40 \times 10^{11} W/cm^2$ , the A peak (might contain three peaks discussed above) move to  $\sim 0.7$  eV due to larger ponderomotive shift. In addition, another small 4-photon peak B appear at  $\sim 1.2$  eV. In (c), with intensity  $60 \times 10^{11} W/cm^2$ , the A peak keep move to lower energy. The small B peak keep steady and we know that this a DRMPI peak from higher energy level (actually it is from 5f discussed above). In (d) and (e), the 4-photon peak at  $\sim 0.7$  eV from 4p and 4f show up which can't be distinguish from other peaks nearby previously due to the broader bandwidth. In (f), with intensity  $120 \times 10^{11} W/cm^2$ , we focus to the 5-photon group (red-dotted line, ranging from 1 eV to 3 eV). Except the one indicated by arrow, all others have a associated 4-photon peaks in front of them which means these 5-photon peaks are the ATI peaks by absorbing one more photon from the front associated 4-photon peaks. We have distinguished two ATI series A's and B's. Therefore, the indicated 5-photon peak with no front associated 4-photon peak should be direct ionized from bound states. This happens when the intensity is so high (so does the ponderomotive shift) that it is no longer enough for ionization by just absorbing 4 photons, one more photon is needed.

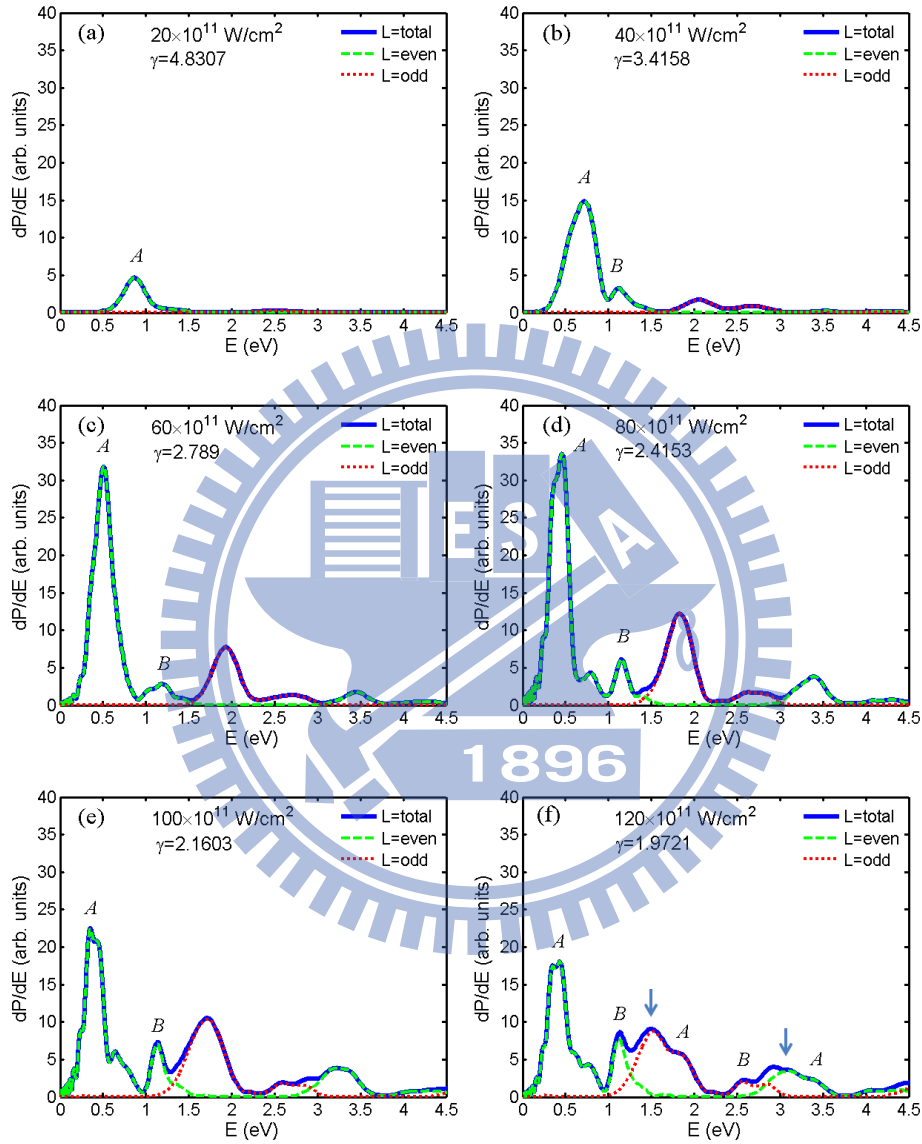


Figure 3.16: Photoelectron spectra of a lithium atom with a linear polarized laser pulse FWHM 10fs, wavelength 785nm, and peak intensity:(a) $20 \times 10^{11} W/cm^2$ , (b) $40 \times 10^{11} W/cm^2$ , (c) $60 \times 10^{11} W/cm^2$ , (d) $80 \times 10^{11} W/cm^2$ , (e) $100 \times 10^{11} W/cm^2$ , and (f) $120 \times 10^{11} W/cm^2$ .



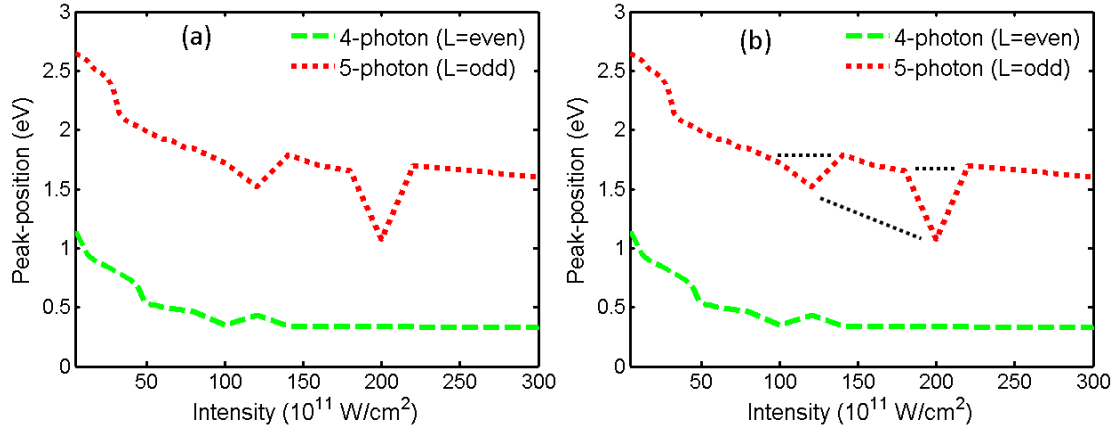


Figure 3.17: (a) peak-position of the highest peak of the 4-photon group (green-dash line) and 5-photon group (red-dotted line) vs laser intensity. (b) the same as (a) with three auxiliary lines.

For more clear, we present the peak-position of the highest peak of the 4-photon group and 5-photon group in Fig 3.17. In (a), we find the highest peak of the 4-photon group decreases with increasing intensity before  $90 \times 10^{11} \text{ W/cm}^2$  due to ponderomotive shift. The highest peak of the 5-photon group is the associated ATI peak of the 4-photon highest peak, hence decreases with 4-photon peak. Their positions differ by about a photon energy (1.57 eV). After  $90 \times 10^{11} \text{ W/cm}^2$ , the intensity is too high to allow direct 4-photon ionization. Therefore, the 4-photon highest peak ceases decrease, but the 5-photon highest peak exhibit a oscillation. After adding some auxiliary lines, see (b), things become clear. As a matter of fact, there exist two paths in the 5-photon highest peak after  $90 \times 10^{11} \text{ W/cm}^2$ . One path is for the associated ATI peak from the front 4-photon highest peak by absorbing one more photon and keep steady as the front 4-photon highest peak, the other is for the direct 5-photon ionization peak and the peak-position continue decrease with increasing intensity. Since these two peaks are both 5-photon peak (in the same order of the perturbation series [77]), they would compete each other and thus exhibit a oscillation as we have observed.

### 3.4 Rydberg stabilization

In this section, we devote to explain the significant change of the behavior of the ionization probability with laser intensity below  $\gamma = 2.5$  that we have mentioned in the section 3.2 (Fig. 3.11). Before proceeding, we discuss atomic stabilization first [78, 79, 80, 81, 82].

The atomic stabilization is easily understood in the Kramers-Henneberger (KH) frame which is the frame of the moving electron in the laser field. The Hamiltonian of an atom interacting with laser field in the length gauge is

$$H = \frac{p^2}{2} + V(r) + \mathbf{E}(t) \cdot \mathbf{r} \quad (3.8)$$

$$\mathbf{E}(t) = E_0 \cos(\omega t) \hat{z} \quad (3.9)$$

where  $\omega$  is the laser frequency and  $E_0$  is the field strength. By doing the following unitary transformation [81]:

$$\left( i \frac{\partial}{\partial t} - H_{KH} \right) = S^{-1} \left( i \frac{\partial}{\partial t} - H \right) S \quad (3.10)$$

where

$$S = \exp(-iT) \quad (3.11)$$

$$T = - \int_0^t \mathbf{A}(t') dt' \left( \frac{1}{i} \frac{\partial}{\partial \mathbf{r}} \right) + \int_0^t \mathbf{A}^2(t') dt' + \mathbf{A} \cdot \mathbf{r} \quad (3.12)$$

We obtain the Kramers-Henneberger Hamiltonian:

$$H_{KH} = \frac{p^2}{2} + V(r - \hat{z} \cdot \alpha \cos(\omega t)) \quad (3.13)$$

where  $\alpha = E_0/\omega^2$  is the amplitude of free-electron oscillation in a laser field.

The oscillating potential in Eq. (3.13) can be expanded in a Fourier series to take the form of a sum of harmonics of the frequency  $\omega$ . The zero-order harmonics, which is the time-averaged part of the sum, represents a stationary potential. When the laser frequency is much higher than the frequency of a atomic state,  $\omega \gg |E_n|/\hbar$ , except the zero-order harmonics, all other higher order terms can be neglected. The KH Hamiltonian is thus independent of time, then the electron is stabilized in that state which is known as KH stabilization.

Rydberg state is not a clearly-defined physical noun. It is usually used to indicate a highly excited state without defining to what extent it should be.

Back to our system, the time scale of the Rydberg states is in microwave range, whereas the 785nm infrared laser is at a much higher frequency than those of microwaves. Then a electron in Rydberg states almost doesn't respond to the laser field and thus is stabilized in those states. This is what we mean "Rydberg stabilization".

It is interesting that stabilization of Rydberg states are accompanied by the transition from direct 4-photon ionization to direct 5-photon ionization. In Fig. 3.18, we show a

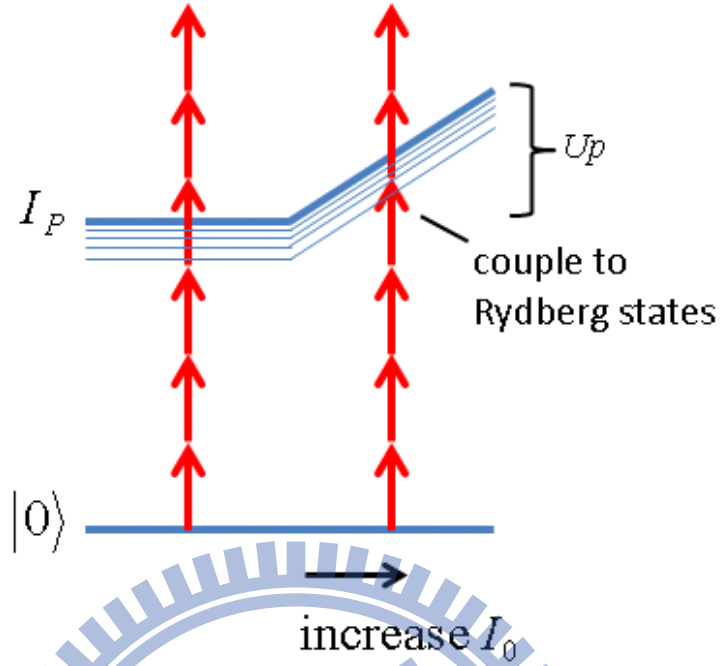


Figure 3.18: Schematic plot of the process of transition from direct 4-photon ionization to direct 5-photon ionization. During this process, it is strongly coupling to Rydberg states.  $|0\rangle$  is the ground state,  $|b\rangle$  is any intermediate bound state,  $IP$  is ionization potential,  $I_0$  is laser intensity,  $Up$  is ponderomotive shift.

schematic plot for the transition process. At smaller intensity, electron can be ionized by absorbing 4 photons. However, with increasing intensity, the ionization threshold (ionization potential plus the ponderomotive shift) rises gradually. Finally, the energy of absorbing 4 photons are lower than the ionization threshold, no longer afford to ionization, but coupling to the Rydberg states instead. From Fig. 3.17, we know that transition from direct 4-photon ionization to direct 5-photon ionization occur at about  $90 \times 10^{11} W/cm^2$  ( $\gamma \sim 2.3$ ). We now proceed to check is there anything happening at ( $\gamma \sim 2.3$ ).

In Fig. 3.19, we show the ionization probability and the sum of the occupation probability of the low-lying bound states with principal quantum number  $n \leq 4$  and those of Rydberg states with  $n \geq 5$  for 30fs, 10fs, and 6fs pulses. We find that there is a dramatic occupation to Rydberg states from ( $\gamma \sim 2.3$ ) for all three cases. We also find that the trend of the ionized probability is closely related to that in the Rydberg states. This manifest itself the Rydberg stabilization indeed dominate the features of the ionization probability below  $\gamma = 2.3$ . The recover and oscillation of ionization probabilities for 10fs and 6fs pulses are due to the broader bandwidth of these shorter pulses. In 30fs case, the narrower bandwidth can concentrate on the Rydberg states and lasts for even higher intensities (smaller  $\gamma$ ). In 10fs case, the energy bandwidth can also concentrate on the

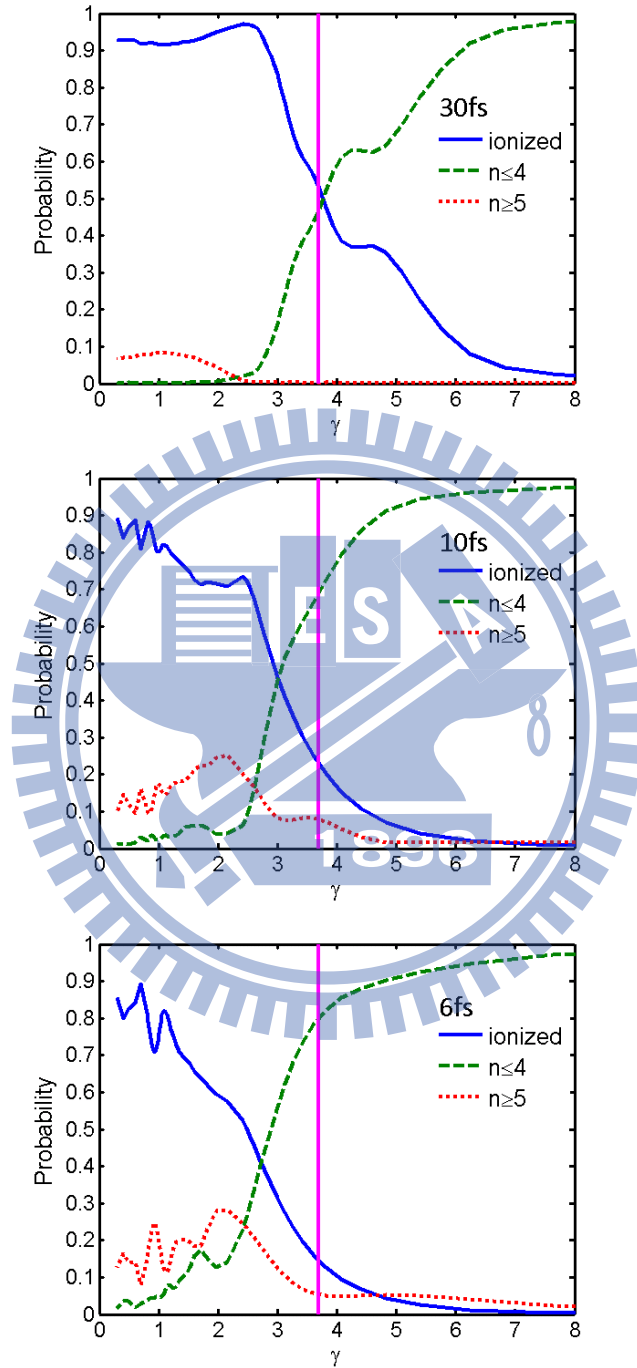


Figure 3.19: Ionization probability and the sum of the occupation probability of the low-lying bound states with principal quantum number  $n \leq 4$  and those of Rydberg states with  $n \geq 5$  for 30fs, 10fs, and 6fs pulses.

Rydberg states at  $\gamma \sim 2.3$ . However, when  $\gamma$  reach to about 1.5. The energy bandwidth start to cover lower levels where electron is no longer stabilized under the laser field and thus ionized [83]. In 10fs case, the broader bandwidth can't concentrate on the Rydberg states only, it always covers the low-lying states. So the phenomena of ionization trapping is not so dramatic as 30fs and 10fs pulses, it only exhibits a reduction of the ionization rate. In addition to Rydberg stabilization, this reduced ionization rate is partially due to the the direct 5-photon ionization dominant in this regime which is the next order to the direct 4-photon ionization of the perturbation series.

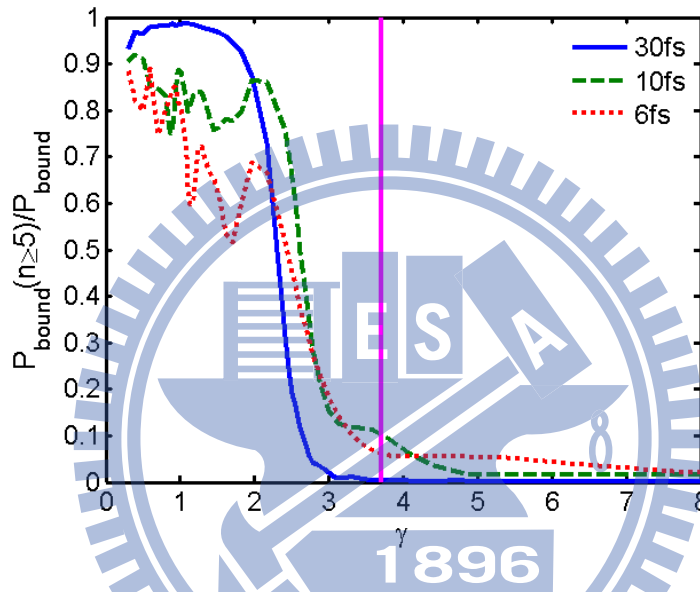


Figure 3.20: Ratio of the sum of the occupation probability of the Rydberg states ( $n \geq 5$ ) to that of total bound states.

In Fig. 3.20, we show the ratio of the sum of the occupation probability of the Rydberg states ( $n \geq 5$ ) to that of total bound states. We find that, at about  $\gamma = 2.3$  (the critical value for transition from direct 4-photon ionization to direct 5-photon ionization), the bound electron dramatically occupy Rydberg states. For 30fs pulse, over 90% bound electron occupy the Rydberg state, over 80% for 10fs pulse, and over 60% for 10fs pulse. This also confirms the Rydberg stabilization. The drop of the ratio of the Rydberg states to the bound states at  $\gamma = 1$  for 30fs pulse is simply because the 4-photon arrow starts to couple to low-lying states with keeping increasing laser intensity.

### 3.5 Fanlike structure in the direction perpendicular to the polarization axis

In this section, we try to explain why the ionized electron is distributed mainly in the direction perpendicular to the polarization axis gradually which have been observed from Fig. 3.7 (e) to (g). Intuitively, electron is driven by the laser field and should be move mainly in the polarization direction. Why the distribution changes to the direction perpendicular to the polarization axis in the higher intensity regime? In Fig. 3.21, we show the two-dimensional momentum distribution for three intensities,  $120 \times 10^{11} W/cm^2$ ,  $200 \times 10^{11} W/cm^2$ , and  $700 \times 10^{11} W/cm^2$ . Rather than according to Eq. (2.29)

$$\frac{\partial^2 P}{\partial E \partial \theta} = \frac{\partial^3 P}{\partial^3 \mathbf{p}} 2\pi p \sin\theta \quad (3.14)$$

which we used previously in this chapter, we just plot  $|\Psi_C|^2$  this time to reveal the electron distribution in the polarization direction. The  $\sin\theta$  in Eq. (3.14) eliminates the probability in the polarization direction where  $\theta = 0, \text{ and } \pi$ , hence Eq. (3.14) is usually used to emphasize the multiphoton rings in the direction perpendicular to the polarization axis. In (a), as expected, we find there has a considerable probability in the polarization direction. In (b), the ionization probability decrease, especially in the polarization direction. Ionization probability keep decreasing in (c). From (a) to (c), we realize that the observed electron distribution mainly in the direction perpendicular to the polarization axis is not because electron becomes ionized more in that direction but the ionization probability decrease more rapidly in the polarization direction instead. As a result, it look like the electron distribution changes to the direction perpendicular to the polarization axis, especially plotted with the form of Eq. (3.14). [refer to Fig. 3.7 (g)]

Interestingly, this phenomena is closely related to the Rydberg stabilization. The "disappeared" electron actually recombined to the bound state. Electron with velocity in the polarization direction is more easy to drive back to the ion core, and thus has more change to recombine. This is why the electron distribution along the polarization axis decrease more rapidly in (b) and (c). In the Rydberg stabilization regime, it is easy to couple to Rydberg states. No matter what states the recombined electron stay, it is almost sent to Rydberg states finally and keep stabilized there. This recombination mechanism also interprets the suppression of the ionization probability below  $\gamma = 2.3$  in Fig. 3.11 for 30fs and 10fs pulses.

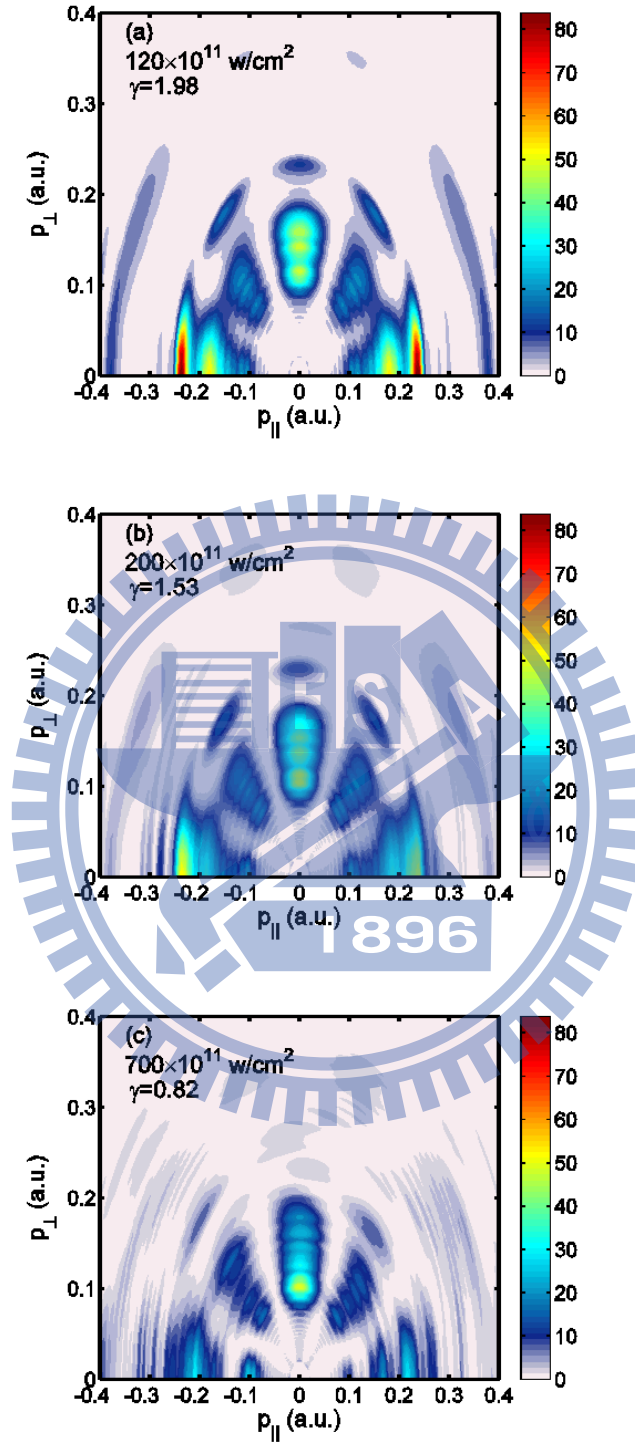


Figure 3.21: Two-dimensional momentum distribution of a lithium atom with a linear polarized laser pulse FWHM 30fs, wavelength 785nm, and peak intensity:(a) $120 \times 10^{11} W/cm^2$ , (b) $200 \times 10^{11} W/cm^2$ , (c) $700 \times 10^{11} W/cm^2$ . In this figure, we just plot  $|\Psi_C|^2$  rather than according to Eq. (3.14) we used previously in this chapter.  $p_{||}$  and  $p_{\perp}$  denote the momentum parallel and perpendicular to polarization axis, respectively.

# Chapter 4

## Conclusion

In the first part of this thesis, we developed an accurate as well as efficient scheme to solve time-dependent Schrödinger equation in momentum space (P-space TDSE) of an atom interacting with a laser field. Our scheme is based on second-order split-operator method in energy representation. The central part of this method is to have an accurate complete eigenstates as well as eigenenergies of the atomic Hamiltonian. However, the singularity in the P-space Coulomb potential make it difficult to solve the eigenvalue equation accurately. Although this singularity can be removed by using Landé subtraction method and solve the eigenvalue equation accurately, there exist another problem. Typical usage of the Landé subtraction require a larger upper bound  $p_{max}$  in momentum space to guarantee the accuracy. This larger upper bound  $p_{max}$  make the time propagation of the P-space TDSE not efficient. We modify the Landé subtraction method to be applicable in a smaller  $p_{max}$ , named "Landé subtraction method with finite integration limits". As a result, accuracy as well as efficiency of the P-space TDSE are both improved greatly. We test the scheme for linear polarized pulse, circular polarized pulse, and long wavelength pulse. Our results agree well with other calculations. In addition, we also apply the Landé subtraction method with finite integration limits to generalize the Lewenstein model by taking scattering process into account. The generalized Lewenstein model corresponding to the sum of all order of the Keldysh-Faisal-Reiss (KFR) theory and thus is a nonperturbative model.

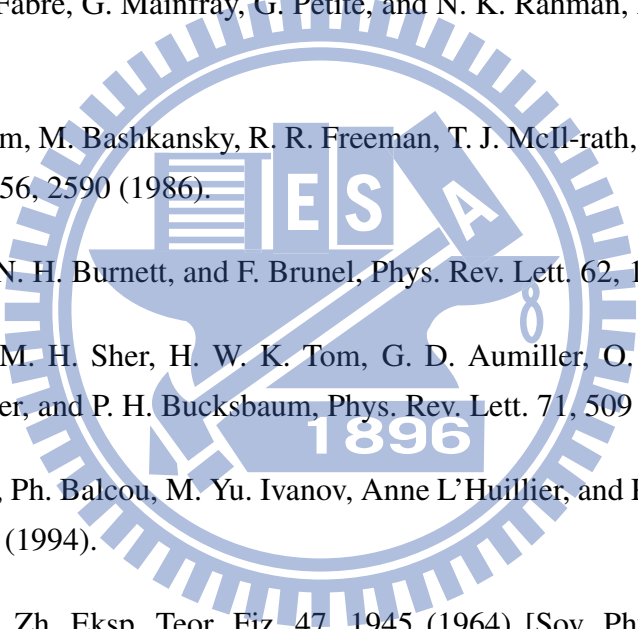
Next, we apply the developed P-space TDSE to study the strong-field ionization of a lithium atom in the single-active-electron approximation. Our results agree well with experimental results. By checking population history of relevant bound states and separation of photoelectron spectra into odd and even angular momentum parts. We can trace the origin of those multiphoton ionization peaks from nonresonant multiphoton ionization (NRMPI) or dynamical resonant multiphoton ionization (DRMPI). We observe a transition from direct 4-photon ionization to direct 5-photon ionization. During this transition



process, Rydberg states are strongly coupled and dramatically occupied due to Kramers-Henneberger stabilization. We also explain why the electron is distributed in the direction perpendicular to the polarization axis in the higher laser intensity regime. Rather than the ionization probability increasing in the perpendicular direction, the electron along the polarization has more changes to recombine to bound state, and finally stabilized in the Rydberg states.



# Bibliography

- 
- [1] T. Brabec and F. Krausz, *Rev. Mod. Phys.* 72, 545 (2000).
- [2] F. Krausz and M. Ivanov, *Rev. Mod. Phys.* 81, 163 (2009).
- [3] P. Agostini, F. Fabre, G. Mainfray, G. Petite, and N. K. Rahman, *Phys. Rev. Lett.* 42, 1127 (1979).
- [4] P. H. Bucksbaum, M. Bashkansky, R. R. Freeman, T. J. McIl-rath, and L. F. DiMauro, *Phys. Rev. Lett.* 56, 2590 (1986).
- [5] P. B. Corkum, N. H. Burnett, and F. Brunel, *Phys. Rev. Lett.* 62, 1259 (1989).
- [6] U. Mohideen, M. H. Sher, H. W. K. Tom, G. D. Aumiller, O. R. Wood II, R. R. Freeman, J. Boker, and P. H. Bucksbaum, *Phys. Rev. Lett.* 71, 509 (1993).
- [7] M. Lewenstein, Ph. Balcou, M. Yu. Ivanov, Anne L'Huillier, and P. B. Corkum, *Phys. Rev. A* 49, 2117 (1994).
- [8] L. V. Keldysh, *Zh. Eksp. Teor. Fiz.* 47, 1945 (1964) [*Sov. Phys. JETP* 20, 1307 (1965)].
- [9] M. Y. Ivanov, M. Spanner, and O. Smirnova, *J. Mod. Opt.* 20, 165 (2005).
- [10] R. R. Freeman, P. H. Bucksbaum, H. Milchberg, S. Darack, D. Schumacher and M. E. Geusic, *Phys. Rev. Lett.* 59, 1092 (1987).
- [11] R. Wiehle, B. Witzel, H. Helm, and E. Cormier, *Phys. Rev. A* 67, 063405 (2003).
- [12] P. Agostini, P. Breger, A. L'Huillier, H. G. Muller, G. Petite, A. Antonetti, and A. Migus, *Phys. Rev. Lett.* 63, 2208 (1989).
- [13] P. Hansch, M. A. Walker, and L. D. Van Woerkom, *Phys. Rev. A* 55, R2535 (1997).
- [14] H. G. Muller and F. C. Kooiman, *Phys. Rev. Lett.* 81, 1207 (1998).

- [15] R. Moshhammer, J. Ullrich, B. Feuerstein, D. Fischer, A. Dorn, C. D. Schröter, J. R. Crespo Lopez-Urrutia, C. Hoehr, H. Rottke, C. Trump, M. Wittmann, G. Korn, and W. Sandner, *Phys. Rev. Lett.* 91, 113002 (2003).
- [16] J. Chen and C. H. Nam, *Phys. Rev. A* 66, 053415 (2002).
- [17] K. I. Dimitriou, D. G. Arbó, S. Yoshida, E. Persson, and J. Burgdörfer, *Phys. Rev. A* 70, 061401(R) (2004).
- [18] F. H. M. Faisal and G. Schlegel, *J. Phys. B* 38, L223 (2005).
- [19] A. Rudenko, K. Zrost, C. D. Schröter, V. L. B. de Jesus, B. Feuerstein, R. Moshhammer, and J. Ullrich, *J. Phys. B* 37, L407 (2004).
- [20] C. M. Maharjan, A. S. Alnaser, I. Litvinyuk, P. Ranitovic, and C. L. Cocke, *J. Phys. B* 39, 1955 (2006).
- [21] A. S. Alnaser, C. M. Maharjan, P. Wang, and I. V. Litvinyuk, *J. Phys. B* 39, L323 (2006).
- [22] C. I. Blaga, F. Catoire, P. Colosimo, G. G. Paulus, H. G. Muller, P. Agostini, and L. F. DiMauro, *Nat. Phys.* 5, 335 (2009).
- [23] W. Quan, Z. Lin, M. Wu, H. Kang, H. Liu, X. Liu, J. Chen, J. Liu, X. T. He, S. G. Chen, H. Xiong, L. Guo, H. Xu, Y. Fu, Y. Cheng, and Z. Z. Xu, *Phys. Rev. Lett.* 103, 093001 (2009).
- [24] F. H. M. Faisal, *Nat. Phys.* 5, 319 (2009).
- [25] C. Liu and K. Z. Hatsagortsyan, *Phys. Rev. Lett.* 105, 113003 (2010).
- [26] T. M. Yan, S. V. Popruzhenko, M. J. J. Vrakking, and D. Bauer, *Phys. Rev. Lett.* 105, 253002 (2010).
- [27] A. Kastner, U. Saalman, and J. M. Rost, *Phys. Rev. Lett.* 108, 033201 (2012).
- [28] C. Lemell, K. I. Dimitriou, X. M. Tong, S. Nagele, D. V. Kartashov, J. Burgdörfer, and S. Gräfe, *Phys. Rev. A* 85, 011403(R) (2012).
- [29] P. Colosimo, G. Doumy, C. I. Blaga, J. Wheeler, C. Hauri, F. Catoire, J. Tate, R. Chirila, A. M. March, G. G. Paulus, H. G. Muller, P. Agostini, and L. F. DiMauro, *Nat. Phys.* 4, 386 (2008).
- [30] R. Nepstad, H. W. van der Hart, and J. F. McCann, *J. Phys. B* 42, 145603 (2009).

- [31] M. Abu-Samha, and L. B. Madsen, *J. Phys. B* 44, 235601 (2011).
- [32] F. H. M. Faisal, *J. Phys. B* 6, L89 (1973).
- [33] H. R. Reiss, *Phys. Rev. A* 22, 1786 (1980).
- [34] X. M. Tong and Shih-I Chu, *Chem. Phys.* 217, 119 (1997).
- [35] M. Nurhuda and F. H. M. Faisal, *Phys. Rev. A* 60, 3125 (1999).
- [36] A. N. Grum-Grzhimailo, B. Abeln, K. Bartschat, D. Weflen, and T. Urness, *Phys. Rev. A* 81, 043408 (2010).
- [37] T. J. Park and J. C. Light, *J. Chem. Phys.* 85, 5870 (1986).
- [38] D. A. Telnov and Shih-I Chu, *Phys. Rev. A* 79, 043421 (2009).
- [39] D. A. Telnov and Shih-I Chu, *Phys. Rev. A* 83, 063406 (2011).
- [40] X. M. Tong, K. Hino, and N. Toshima, *Phys. Rev. A* 74, 031405(R) (2006).
- [41] X. M. Tong, S. Watahiki, K. Hino, and N. Toshima, *Phys. Rev. Lett.* 99, 093001 (2006).
- [42] Liang Tao and A. Scrinzi, *New J. Phys.* 14, 013021 (2012).
- [43] Z. Zhou, and Shih-I Chu, *Phys. Rev. A* 83, 013405 (2011).
- [44] T. F. Jiang, S. D. Jheng, Y. M. Lee, and Z. Y. Su, *Phys. Rev. E* 86, 066702 (2012).
- [45] S. D. Jheng, and T. F. Jiang, *J. Phys. B* 46, 115601 (2013).
- [46] Zheng Zhang, Liang-You Peng, Qihuang Gong, and Toru Morishita, *Optics Express* 18, 8976 (2010).
- [47] Zheng Zhang, Liang-You Peng, Ming-Hui Xu, Anthony F. Starace, Toru Morishita, and Qihuang Gong, *Phys. Rev. A* 84, 043409 (2011).
- [48] Chien-Nan Liu, Akiyoshi Hishikawa, and Toru Morishita, *Phys. Rev. A* 86, 053426 (2012).
- [49] C. Ruiz, L. Plaja, and L. Roso, *Phys. Rev. Lett.* 94, 063002 (2005).
- [50] A. Emmanouilidou, V. Hakobyan, and P. Lambropoulos, *J. Phys. B* 46, 111001 (2013).

- [51] M. Schuricke, Ganjun Zhu, J. Steinmann, K. Simeonidis, I. Ivanov, A. Kheifets, A. N. Grum-Grzhimailo, K. Bartschat, A. Dorn, and J. Ullrich, *Phys. Rev. A* 83, 023413 (2011).
- [52] Z. Chen, T. Morishita, A.-T. Le, M. Wickenhauser, X. M. Tong and C. D. Lin, *Phys. Rev. A* 74, 053405 (2006).
- [53] D. G. Arbo, S. Yoshida, E. Persson, K. I. Dimitriou, and J. Burgdorfer, *Phys. Rev. Lett.* 96, 143003 (2006).
- [54] M. Wickenhauser, X.M. Tong, and C. D. Lin, *Phys. Rev. A* 73, 011401(R) (2006).
- [55] Y. R. Kwon and F. Tabakin *Phys. Rev. C* 18, 932 (1978).
- [56] I. A. Ivanov and J. Mitroy, *Comput. phys. Commun.* 134, 317 (2001).
- [57] H. A. Bethe and E. E. Salpeter, *Quantum Mechanics of One- and Two-Electron Atoms* (Plenum, New York, 1977).
- [58] B. H. Bransden and C. J. Joachain, *Physics of atoms and molecules*, 2nd ed. (Prentice Hall, New York, (2003).
- [59] Z. Chen, T. Morishita, A.-T. Le, and C. D. Lin, *Phys. Rev. A* 76, 043402 (2007).
- [60] A. Sarsa, F. J. Gálvez, and E. Buendia, *At. Data Nucl. Data Tables* 88, 163 (2004).
- [61] X. M. Tong and C. D. Lin, *J. Phys. B* 38, 2593 (2005).
- [62] H. B. Dwight, *Tables of Integrals and Other Mathematical Data*, 4th ed. (Macmillan, New York, 1966).
- [63] T. F. Jiang, *Comp. Phys. Commun.* 178, 571 (2008).
- [64] J. Wang, Shih-I Chu, and C. Laughlin, *Phys. Rev. A* 50, 3208 (1994).
- [65] M. Abu-Samha, and L. B. Madsen, *Phys. Rev. A* 84, 023411 (2011).
- [66] J. J. Sakurai, *Modern Quantum Mechanics*, Revised ed. (Addison Wesley, 1994).
- [67] Zenghu Chang, *Fundamentals of Attosecond Optics* (CRC, Boca Raton, 2011).
- [68] C. D. Lin, S. C. Soong, and L. N. Tunnell, *Phys. Rev. A* 17, 1646 (1978).
- [69] V. P. Krainov and B. Shokri, *JETP* 80, 657 (1995).
- [70] V. P. Krainov, *J. Opt. Soc. Am. B* 14, 425 (1997).

- [71] T. Morishita, Z Chen, S. Watanabe and C. D. Lin, Phys. Rev. A 75, 023407 (2007).
- [72] M. A. Walker, P. Hansch, and L. D. Van Woerkom, Phys. Rev. A 57, R701 (1998).
- [73] W. Schweizer, P. FaßBINDER and R. González-Férez, Atomic Data and Nuclear Data Tables 72, 33 (1999).
- [74] Shih-I Chu and J. Cooper, Phys. Rev. A 32, 2769 (1985).
- [75] M. Wickenhauser, X. M. Tong, D. G. Arbó, J. Burgdörfer, and C. D. Lin, Phys. Rev. A 74, 041402(R) (2006).
- [76] N. B. Delone and V. P. Krainov, Phys Usp 42, 669 (1999).
- [77] F. H. M. Faisal, Theory of Multiphoton Process (Plenum, New York, 1987).
- [78] M. Pont and Gavrilá, Phys. Rev. Lett. 65, 2362 (1990).
- [79] J. H. Eberly<sup>1</sup> and K. C. Kulander, Science 19, 1229 (1993).
- [80] T. F. Jiang, Phys. Rev. A 48, 3995 (1993).
- [81] A. M. Popov, O. V. Tikhonova, and E. A. Volkova, J. Phys. B 36, R125 (2003).
- [82] T. Morishita, and C. D. Lin, Phys. Rev. A 87, 063405 (2013).
- [83] R. R. Jones, Phys. Rev. Lett. 74, 1091 (1995).

# Appendix

## .1 Dipole approximation, velocity gauge, length gauge, and Volkov state

The general expression of the Schrödinger equation of an atom in the laser field can be written as:

$$\begin{aligned} i\hbar \frac{\partial}{\partial t} \Psi(\mathbf{r}, t) &= \left[ \frac{[p + e\mathbf{A}(\mathbf{r}, t)]^2}{2m} + V(r) \right] \Psi(\mathbf{r}, t) \\ &= \left[ H_0 + \frac{e}{m} \mathbf{A}(\mathbf{r}, t) \cdot \mathbf{p} + \frac{e^2}{2m} \mathbf{A}^2(\mathbf{r}, t) \right] \Psi(\mathbf{r}, t) \end{aligned} \quad (1)$$

where  $H_0 = p^2/2 + V(r)$ ,  $\mathbf{A}(\mathbf{r}, t)$  is the vector potential of the laser field,  $V(r)$  is the atomic potential, and the electron charge is defined as  $-e$ . Provided the laser intensity is weak enough that the laser-atom interaction energy is less than the atomic potential energy, the length scale of a electron motion should be in the order of several  $\text{\AA}$ . For a laser in the infrared regime, 800nm for example, the ratio of the length scale of a electron motion and the wavelength of the laser field is too small ( $1\text{\AA}/800nm$ ) that a electron almost doesn't feel the variation of the laser field in the coordinate space. Therefore, the coordinate dependence of the laser field can be neglected where  $\mathbf{A}(\mathbf{r}, t) = \mathbf{A}(t)$ . This is called dipole approximation.

The Schrödinger equation can be simplified by gauge transformation. Two of the often used gauge transformations are velocity gauge and length gauge. If we rewrite the wave function in Eq. (1) with a phase factor as following:

$$\Psi(\mathbf{r}, t) = \exp \left[ -i \frac{1}{\hbar} \frac{e^2}{2m} \int^t \mathbf{A}^2(t') dt' \right] \Psi^V(\mathbf{r}, t) \quad (2)$$

and substitute into Eq. (1), we get the Schrödinger equation of an atom in the laser field in the velocity gauge.

$$i\hbar \frac{\partial}{\partial t} \Psi^V(\mathbf{r}, t) = \left[ H_0 + \frac{e}{m} \mathbf{A} \cdot \mathbf{p} \right] \Psi^V(\mathbf{r}, t) \quad (3)$$

If rewriting the wave function with another phase factor:

$$\Psi(\mathbf{r}, t) = \exp \left[ -i \frac{e}{\hbar} \mathbf{A} \cdot \mathbf{r} \right] \Psi^L(\mathbf{r}, t) \quad (4)$$

we get the Schrödinger equation of an atom in the laser field in the length gauge.

$$i\hbar \frac{\partial}{\partial t} \Psi^L(\mathbf{r}, t) = [H_0 + e\mathbf{E} \cdot \mathbf{r}] \Psi^L(\mathbf{r}, t) \quad (5)$$

Next, we solve the Schrödinger equation of an electron in the laser field. This can be solved exactly and the states are called Volkov states [58]. The Schrödinger equation of an electron in the laser field in the velocity gauge is:

$$i\hbar \frac{\partial}{\partial t} \Psi^V(\mathbf{r}, t) = \left[ \frac{p^2}{2} + \frac{e}{m} \mathbf{A} \cdot \mathbf{p} \right] \Psi^V(\mathbf{r}, t) \quad (6)$$

Then, we let

$$\Psi^V(\mathbf{r}, t) = \exp(i\mathbf{p} \cdot \mathbf{r}) f(t) \quad (7)$$

After substituting into Eq. (6), we get a differential equation for  $f(t)$ :

$$i\hbar \frac{d}{dt} f(t) = \left[ \frac{\hbar^2 p^2}{2m} + \frac{e\hbar}{m} \mathbf{p} \cdot \mathbf{A}(t) \right] f(t) \quad (8)$$

This can be integrated easily:

$$f(t) = C \exp \left[ \frac{-i\hbar p^2 t}{2m} - i\mathbf{p} \cdot \alpha(t) \right] \quad (9)$$

where  $\alpha = \frac{e}{m} \int^t \mathbf{A}(t') dt'$  is quiver amplitude of an electron in the laser field. Substitute back to Eq. (7), and choose the normalization factor to be  $(1/2\pi)^{3/2}$ , then the Volkov states in velocity gauge is

$$\Psi^V(\mathbf{r}, t) = \frac{1}{(2\pi)^{3/2}} \exp(i\mathbf{p} \cdot \mathbf{r}) \exp \left[ \frac{-i\hbar p^2 t}{2m} - i\mathbf{p} \cdot \alpha(t) \right] \quad (10)$$

According to Eq. (2)

$$\Psi(\mathbf{r}, t) = \frac{1}{(2\pi)^{3/2}} \exp(i\mathbf{p} \cdot \mathbf{r}) \exp[-iS_{\mathbf{p}}(t)] \quad (11)$$

where

$$S_{\mathbf{p}}(t) = \frac{1}{2} \int_{-\infty}^{\infty} dt' [\mathbf{p} + \mathbf{A}(t')]^2 \quad (12)$$

And, according to Eq. (4), the Volkov states in length gauge is given by

$$\Psi^L(\mathbf{r}, t) = \frac{1}{(2\pi)^{3/2}} \exp[i(\mathbf{p} + \mathbf{A}(t)) \cdot \mathbf{r}] \exp[-iS_{\mathbf{p}}(t)] \quad (13)$$

where

$$S_{\mathbf{p}}(t) = \frac{1}{2} \int_{-\infty}^{\infty} dt' [\mathbf{p} + \mathbf{A}(t')]^2 \quad (14)$$